The kinesin Kif21b regulates radial migration of cortical projection neurons through a non-canonical function on actin cytoskeleton

José Rivera Alvarez, Laure Asselin, Peggy Tilly, Roxane Benoit, Claire Batisse, Ludovic Richert, Julien Batisse, Bastien Morlet, Florian Levet, Noémie Schwaller, et al.

▶ **To cite this version:**

José Rivera Alvarez, Laure Asselin, Peggy Tilly, Roxane Benoit, Claire Batisse, et al.. The kinesin Kif21b regulates radial migration of cortical projection neurons through a non-canonical function on actin cytoskeleton. Cell Reports, 2023, 42 (7), pp.112744. 10.1016/j.celrep.2023.112744 . hal-04163589

HAL Id: hal-04163589
https://hal.science/hal-04163589

Submitted on 3 Nov 2023

HAL is a multi-disciplinary open access archive for the deposit and dissemination of scientific research documents, whether they are published or not. The documents may come from teaching and research institutions in France or abroad, or from public or private research centers.

L'archive ouverte pluridisciplinaire **HAL**, est destinée au dépôt et à la diffusion de documents scientifiques de niveau recherche, publiés ou non, émanant des établissements d'enseignement et de recherche français ou étrangers, des laboratoires publics ou privés.

Cell Reports

Article

The kinesin Kif21b regulates radial migration of cortical projection neurons through a non-canonical function on actin cytoskeleton

Graphical abstract

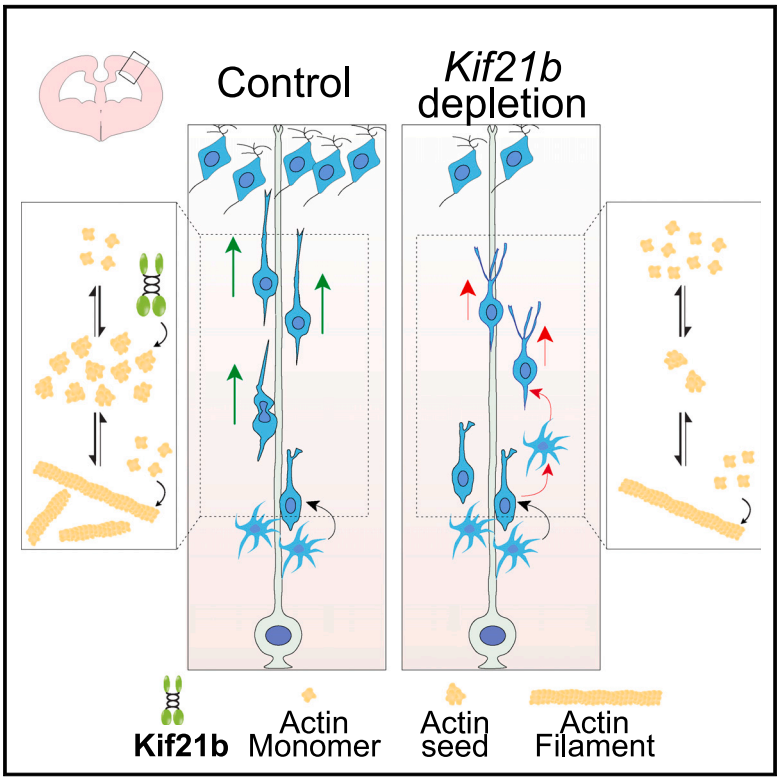

Authors

José Rivera Alvarez, Laure Asselin, Peggy Tilly, ..., Marc Ruff, Anne-Cécile Reymann, Juliette D. Godin

Correspondence

godin@igbmc.fr

In brief

Rivera Alvarez et al. show that the kinesin Kif21b regulates the migration of cortical neurons independently of its well-characterized motility function on microtubules. The authors demonstrate that Kif21b is an actin-binding protein that modulates both actin dynamics and actomyosin contraction in migrating neurons.

Highlights

- Kif21b regulates neuronal migration independently of its motility on microtubules
- Kif21b regulates actin cytoskeleton dynamics through direct binding
- Kif21b function during nucleokinesis relies on the regulation of the actomyosin network
- Kif21b fine-tunes actin dynamics during pausing and branching of migrating neurons

Rivera Alvarez et al., 2023, Cell Reports *42*, 112744
July 25, 2023 © 2023 The Author(s).
https://doi.org/10.1016/j.celrep.2023.112744

CellPress

Cell Reports

CellPress
OPEN ACCESS

Article

The kinesin Kif21b regulates radial migration of cortical projection neurons through a non-canonical function on actin cytoskeleton

José Rivera Alvarez,[1,2,3,4,8] Laure Asselin,[1,2,3,4,8] Peggy Tilly,[1,2,3,4] Roxane Benoit,[1,2,3,4] Claire Batisse,[1,2,3,4] Ludovic Richert,[4,5] Julien Batisse,[1,2,3,4] Bastien Morlet,[1,2,3,4] Florian Levet,[6,7] Noémie Schwaller,[1,2,3,4] Yves Mély,[4,5] Marc Ruff,[1,2,3,4] Anne-Cécile Reymann,[1,2,3,4] and Juliette D. Godin[1,2,3,4,9,*]

[1]Institut de Génétique et de Biologie Moléculaire et Cellulaire, IGBMC, 67404 Illkirch, France
[2]Centre National de la Recherche Scientifique, CNRS, UMR7104, 67404 Illkirch, France
[3]Institut National de la Santé et de la Recherche Médicale, INSERM, U1258, 67404 Illkirch, France
[4]Université de Strasbourg, 67000 Strasbourg, France
[5]Laboratoire de Bioimagerie et Pathologies, Centre National de la Recherche Scientifique, UMR 7021, 67404 Illkirch, France
[6]University of Bordeaux, CNRS, UMR 5297, Interdisciplinary Institute for Neuroscience, IINS, 33000 Bordeaux, France
[7]University of Bordeaux, CNRS, INSERM, Bordeaux Imaging Center, BIC, UAR 3420, US 4, 33600 Pessac, France
[8]These authors contributed equally
[9]Lead contact
*Correspondence: godin@igbmc.fr
https://doi.org/10.1016/j.celrep.2023.112744

SUMMARY

Completion of neuronal migration is critical for brain development. Kif21b is a plus-end-directed kinesin motor protein that promotes intracellular transport and controls microtubule dynamics in neurons. Here we report a physiological function of Kif21b during radial migration of projection neurons in the mouse developing cortex. *In vivo* analysis in mouse and live imaging on cultured slices demonstrate that Kif21b regulates the radial glia-guided locomotion of newborn neurons independently of its motility on microtubules. We show that Kif21b directly binds and regulates the actin cytoskeleton both *in vitro* and *in vivo* in migratory neurons. We establish that Kif21b-mediated regulation of actin cytoskeleton dynamics influences branching and nucleokinesis during neuronal locomotion. Altogether, our results reveal atypical roles of Kif21b on the actin cytoskeleton during migration of cortical projection neurons.

INTRODUCTION

The cerebral cortex is a central structure of the mammalian brain that commands all higher-order functions. It contains specialized types of excitatory projection neurons, inhibitory interneurons, and glia that are distributed within layers and are regionally organized into areas responsible for motor, sensory, and cognitive functions.[1–3] Proper functioning of the neocortex depends on the active migration of the two major classes of cortical neurons, the pyramidal projection neurons that primarily engage in radial migration[4] and the GABAergic interneurons that undergo tangential migration.[5] Consequently, in human, abnormal cortical layering leads to cortical malformation and is often associated with epilepsy and intellectual disability.[6–9]

To reach their final position in the cortical plate, projection neurons first undergo somal translocation and then, as the cortical wall thickens, they switch to a multimodal radial migration that is accompanied by a series of highly coordinated morphological changes.[10,11] Newborn projection neurons first adopt a multipolar morphology and migrate randomly in the intermediate zone.[12,13] Then they undergo a multipolar-to-bipolar transition to initiate locomotion along the radial glia scaffold. During this locomotion phase, the displacement of projection neurons is paced by successive cycles of nucleokinesis,[14–16] as well as occasional pauses.[17] Once the glia-guided locomotion is completed, the projection neurons connect to the pia and undergo a final somal translocation to settle at appropriate position in the cortical plate.[10] Most of the identified mechanisms underlying the different steps of radial migration ultimately converge on the dynamic remodeling of both microtubule (MT) and actin cytoskeletons.[18–21] Further reflecting the importance of these cytoskeletons in the regulation of radial migration, variants in genes encoding for tubulin subunits, actin components, MT-associated proteins, actin-binding proteins, or motor proteins have been largely associated with neuronal migration disorders.[9,22]

Kif21b is a kinesin particularly enriched in the brain from early development onward[23–25] that promotes intracellular transport along MTs[26–31] and controls MT dynamics.[26,27,29,30,32,33] In particular, Kif21b accumulates at the MT plus ends, where it stabilizes assembled MT by limiting MT polymerization and suppressing catastrophes.[26,30,32,33] During cortical development, Kif21b is specifically expressed in postmitotic neurons, where it localizes in dendrites, axons, and growth cones.[24,25,34]

This is an open access article under the CC BY-NC-ND license (http://creativecommons.org/licenses/by-nc-nd/4.0/).

Depletion of Kif21b *in vivo* in mice leads to severe brain malformations, including microcephaly, hydrocephaly, and dysgenesis of the corpus callosum,[35] as well as deficits in learning, memory, and social behavior[27,28,36] and impaired neuronal maturation and synaptic function.[27,36,37] Although these results clearly point to critical roles of Kif21b in brain development and function, the underlying cellular and molecular mechanisms have not been elicited yet.

Pathological variants in *KIF21B* have been identified in patients presenting with brain malformation and intellectual disability.[25,38] Interestingly, those variants impair neuronal migration and interhemispheric connectivity by enhancing KIF21B canonical motor activity through a gain-of-function mechanism.[25,38] In addition, haploinsufficient *KIF21B* variant also leads to migratory defects, suggesting that dosage of KIF21B is critical for neuronal migration,[25] the exact underlying molecular mechanisms of which remain elusive.

Here we uncover the physiological roles of Kif21b during radial migration of cortical projection neurons. By combining *in vivo* genetic perturbation in mouse cortices, complementation assays, and time-lapse recording on organotypic brain slices, we show that the kinesin Kif21b is required to maintain bipolar morphology and to promote nucleokinesis and dynamic branching of cortical projection neurons during glia-guided locomotion. The canonical motor activity of Kif21b is dispensable for its function in migrating neurons. We demonstrate that Kif21b controls radial migration partly by regulating actin cytoskeleton dynamics through its direct binding to actin filaments. Altogether our data identify a non-canonical function of Kif21b on actin cytoskeleton participating in the regulation of cortical neuron migration.

RESULTS

Kif21b is cell autonomously required for radial migration of projection neurons

To explore the function of Kif21b on neuronal migration, we assessed the consequences of acute depletion of *Kif21b* specifically in postmitotic neurons using *in utero* electroporation (IUE) of CRE-dependent inducible short hairpin RNA (shRNA) vectors,[39] together with two plasmids allowing expression of CRE or GFP under the control of the NeuroD promoter (NeuroD:CRE and NeuroD:GFP, respectively) in mouse embryonic cortices. Efficacy of the two shRNAs was confirmed by western blot in the HEK-293T cell line (−93.4% for sh-*Kif21b* #1 and −61.4% for sh-*Kif21b* #2 when compared with Kif21b expression in Scramble-transfected cells) (Figures S1A and S1B). The depletion of endogenous *Kif21b* was confirmed by Kif21b immunolabeling in primary cortical neurons at day *in vitro* (DIV) 4, 3 days after transfection of the sh-*Kif21b* #2 and NeuroD:CRE (Figures S1C and S1D). As described previously,[25] the distribution of GFP-positive (GFP+) layer 4 neurons silenced for *Kif21b* by IUE at embryonic day (E) 14.5 was significantly impaired with a notable reduction of GFP^+ neurons reaching the upper cortical plate (Up CP) at E18.5 upon acute depletion of *Kif21b* compared with control (−19.4% for sh-*Kif21b* #1, −30% for sh-*Kif21b* #2) (Figures 1A, 1B, S1E, and S1F). *Kif21b*-depleted projection neurons arrested in the intermediate zone expressed the upper-layer marker Cux1, supporting a faulty neuronal migration rather than specification defects (Figure 1C). Of note, *Kif21b*-silenced and control layer 4 projection neurons showed similar distribution in the cortical plate after birth, arguing for a delay in migration rather than a permanent arrest.[25] Because a significant fraction of *Kif21b*-depleted neurons were arrested in the ventricular and subventricular zones, we further tested whether depletion of *Kif21b* could non-cell-autonomously affect the progenitors' biology. We performed IUE of inducible sh-*Kif21b* #2 and NeuroD:CRE at E14.5 and analyzed the total number and the proliferative fraction ($Ki67^+$) of both apical ($Pax6^+$) and intermediate progenitors ($Tbr2^+$) at E16.5 (Figures S1G–S1L). These analyses did not reveal any differences between neuron-specific *Kif21b* depletion and control condition, excluding the non-cell-autonomous effect of *Kif21b* depletion on progenitors.

To investigate the migration of other subtypes of cortical projection neurons, we performed IUE of sh-*Kif21b* #2 and NeuroD:CRE at E13.5 and E15.5 and analyzed the distribution of layer 5 and layer 2/3 neurons at E18.5 and post-natal day (P) 2, respectively. Like for the L4 neurons, radial migration of the layer 2/3 neurons was altered upon *Kif21b* depletion (Figures 1D and 1E). On the contrary, silencing of *Kif21b* did not affect the migration of layer 5 projection neurons (Figures 1F and 1G), suggesting that Kif21b specifically regulates radial migration of upper-layer neurons.

Because Kif21a, the other member of the kinesin-4 family, shares a high sequence similarity with Kif21b,[24] we tested whether the two paralogues have redundant function in neuronal migration. We assessed the ability of mouse wild-type (WT) Kif21b or Kif21a proteins to restore migration defects induced by *Kif21b* knockdown. We performed co-electroporation of plasmids expressing Kif21b or Kif21a under the regulation of the neuronal NeuroD promotor together with NeuroD-driven sh-*Kif21b* #2 that targets the 3′ UTR of endogenous *Kif21b* transcripts (Figure S1B) at E14.5. Whereas Kif21b fully restored the defective migration induced by sh-*Kif21b* #2, co-electroporation of Kif21a failed to rescue the impaired distribution of *Kif21b*-depleted neurons (Figures 1A, 1B, S3B, and S3C), suggesting that loss of Kif21b function in migrating neurons cannot be compensated by Kif21a. Notably, Kif21b likely regulated neuronal migration in a cell-autonomous manner because *Kif21b* silencing did not affect cell survival (Figure S1M) and glia scaffold integrity (Figure S1N). Finally, we investigated the migration phenotype in $Kif21b^{flox/flox}$ conditional knockout (KO; cKO) embryos by IUE of NeuroD:Cre and NeuroD:GFP plasmids at E14.5. We confirmed the impaired positioning of *Kif21b* KO neurons 4 days after IUE, with a reduction of 13.9% of neurons distributed in the Up CP in $Kif21b^{flox/flox}$ compared with $Kif21b^{WT/WT}$ embryos (Figures 1H and 1I).

Given the expression of Kif21b in the mouse developing ganglionic eminences where the cortical inhibitory GABAergic neurons are born (Figures S2A and S2B), we asked whether Kif21b also regulates tangential migration of interneurons. We performed *in vitro* culture of medial ganglionic explants (MGEs) from E13.5 Dlx:Cre-GFP embryos electroporated *ex vivo* with Cre-dependent cherry-expressing vector (pCAG-loxPSTOPloxP-Cherry) together with CRE-inducible sh-scramble or sh-*Kif21b* #2 on a layer of WT cortical feeders.

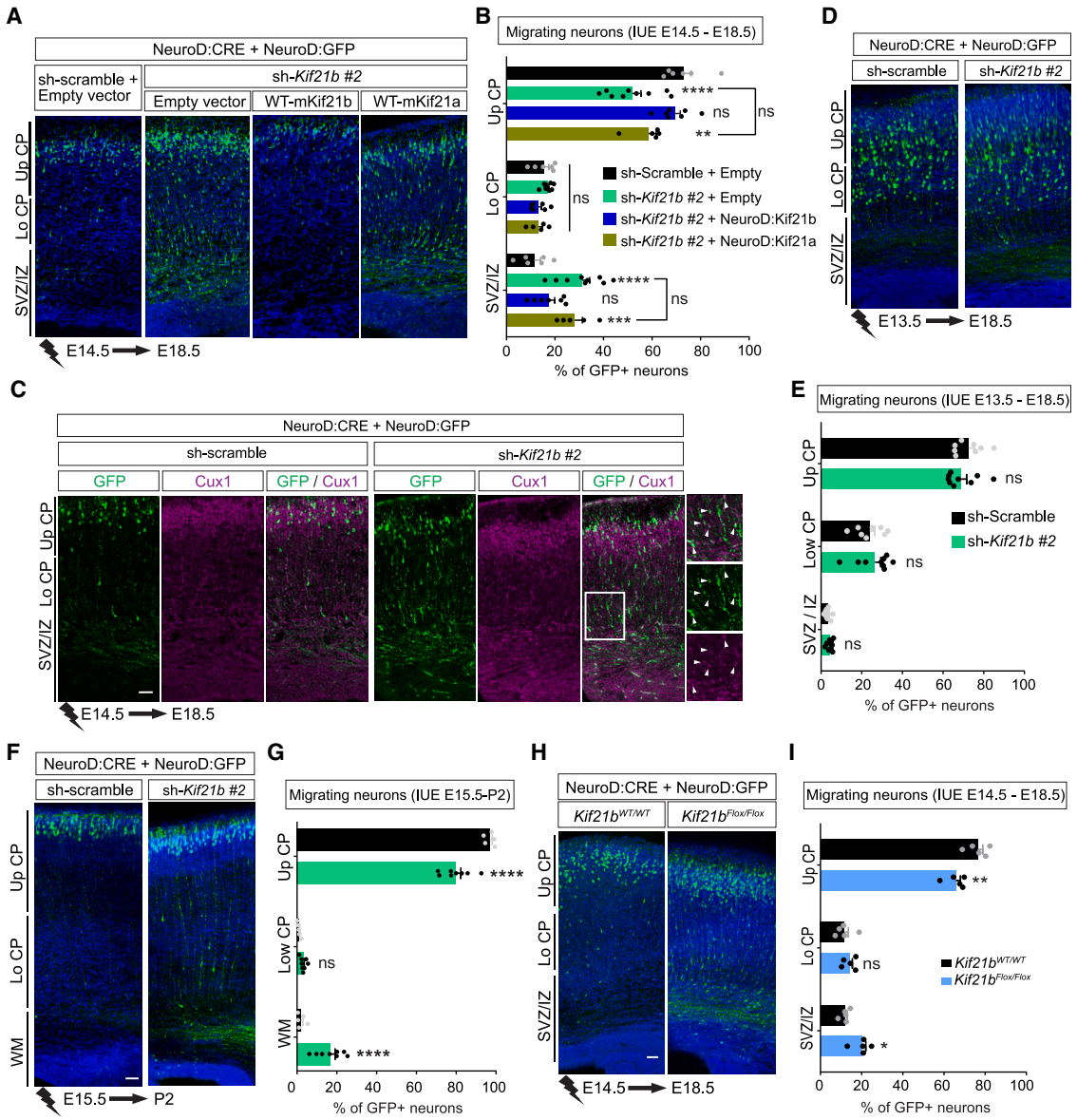

Figure 1. Kif21b is cell autonomously required for radial migration of projection neurons

(A, D, and F) Coronal sections of E18.5 (A and D) or P2 (F) mouse cortices electroporated at E14.5 (A), E13.5 (D), or E15.5 (F) with NeuroD:Cre and NeuroD:IRES-GFP, together with either Cre-inducible shRNA-*Kif21b* #2 in combination with NeuroD-driven indicated constructs.

(C) Cux1 immunostaining (red) of E18 mouse cortices electroporated at E14.5 with indicated constructs showing correct specification of GFP-positive *Kif21b*-depleted arrested neurons (arrowheads in insets).

(H) Coronal sections of E18.5 WT or floxed *Kif21b* conditional knockout ($Kif21b^{flox/flox}$) mouse cortices electroporated at E14.5 with NeuroD:Cre and NeuroD:IRES-GFP.

(A, D, F, and H) GFP-positive electroporated neurons are depicted in green. Nuclei are stained with DAPI.

(B, E, G, and I) Histograms (means ± SEM) showing the distribution of GFP-positive neurons in different regions.

Significance was calculated by two-way ANOVA, Bonferroni's multiple comparisons test. *$p < 0.05$, **$p < 0.005$, ***$p < 0.001$, ****$p < 0.0001$. Number of embryos analyzed: $n \geq 5$. Scale bars, 50 μm (A, C, D, F, and H). Lo CP, lower cortical plate; ns, non-significant; SVZ/IZ, subventricular zone/intermediate zone; Up CP, upper cortical plate; WM, white matter. See also Figures S1 and S2.

This strategy allows concomitant knockdown of *Kif21b* and expression of a cherry fluorescent reporter specifically in migrating cortical interneurons. Time-lapse recordings of electroporated explants revealed that, although *Kif21b*-silenced interneurons were able to migrate out of the explant, their kinetics of migration were different from the sh-scramble electroporated interneurons (Figures S2C and S2D), with a decreased migration velocity of 24.3%. Altogether, our results revealed the kinesin Kif21b as a key regulator of migration of the two main classes of cortical neurons.

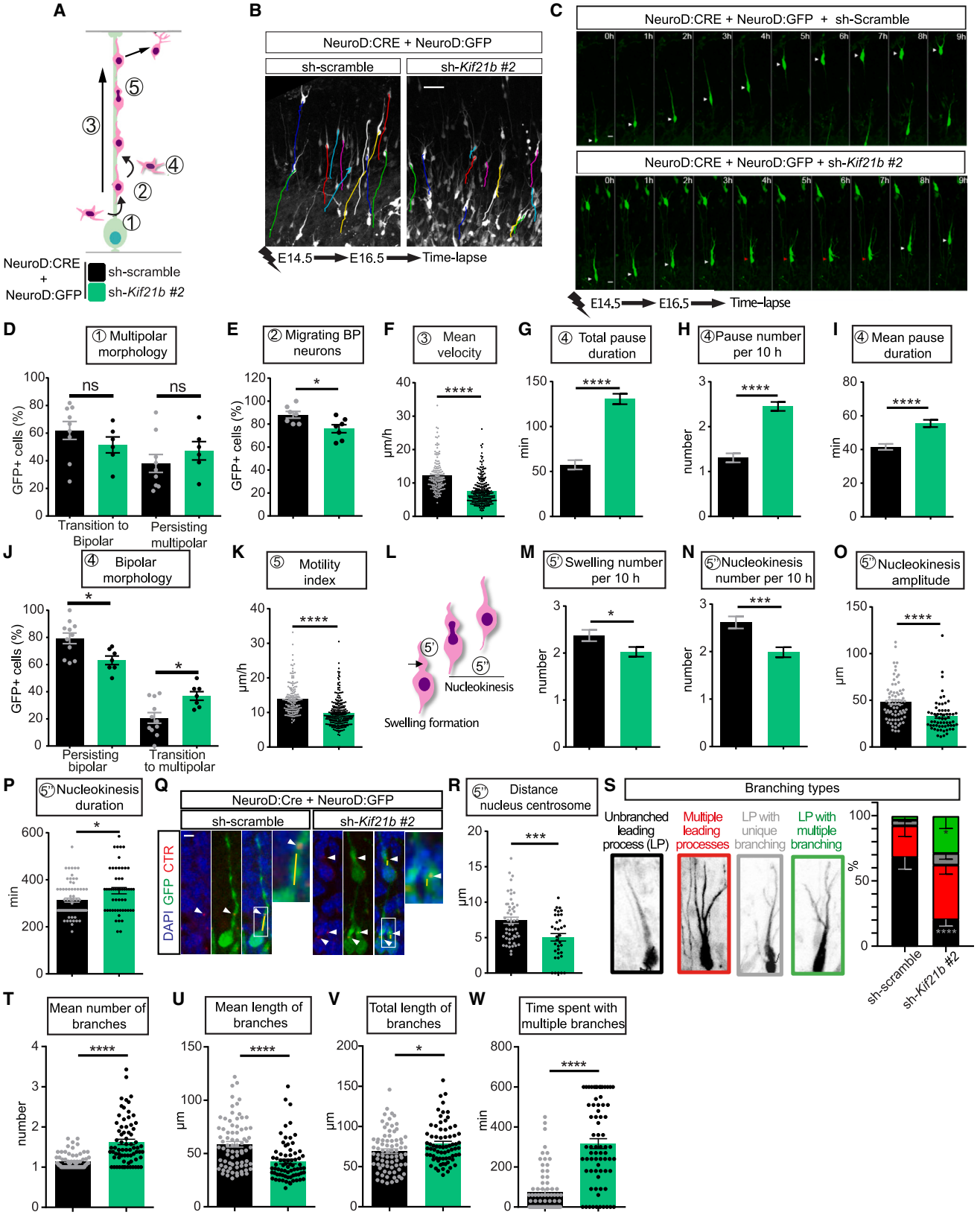

(legend on next page)

Kif21b depletion impedes glia-guided locomotion of projection neurons

To determine how Kif21b controls migration of cortical projection neurons, we further investigated the dynamic cell shape remodeling occurring at the successive steps of migration along radial glia fibers (Figure 2A) by time-lapse recording. IUE of inducible *Kif21b* shRNA or sh-scramble, together with NeuroD:Cre and NeuroD:GFP plasmids, was performed in WT E14.5 embryos. Two days later, brain organotypic slices were cultured *in vitro*, and GFP$^+$ neurons were recorded the next day for 10 h (Figures 2B and 2C). Although *Kif21b* depletion did not affect the initial multipolar-to-bipolar transition required to start glia-guided locomotion (Figures 2A, step 1, and 2D), the percentage of bipolar neurons that actively initiated the locomotory phase was decreased by 13.8% in sh-*Kif21b* #2 condition compared with sh-scramble control (76% and 88.1%, respectively) (Figures 2A, step 2, and 2E). Moreover, the *Kif21b*-silenced bipolar neurons that started glia-guided locomotion (step 3 in Figure 2A) migrated significantly slower (Figures 2B, 2C, and 2F) and spent more time pausing (Figures 2C and 2G). Exacerbated pausing was due to increase in both frequency (Figure 2H) and duration of the pauses (Figure 2I), associated with a loss of bipolar polarity as shown by *Kif21b*-depleted neurons converting more often to multipolar shape while pausing (step 4 in Figures 2A and 2J). Interestingly, the motility index, defined as the velocity during active locomotion excluding the pauses, was decreased in *Kif21b*-silenced neurons (step 5 in Figures 2A and 2K), demonstrating that Kif21b regulates both pausing and effective processivity of migrating projection neurons.

To properly migrate, projection neurons rely on repetitive cycles of forward progression of the cell body that starts with the translocation of a cytoplasmic dilatation (also known as a swelling) in the proximal region of the extending leading process (step 5′ in Figure 2L), and that is followed by the nuclear translocation (hereafter called nucleokinesis) toward the cytoplasmic swelling[40] (step 5″ in Figure 2L). *Kif21b*-silenced neurons form fewer swellings and undergo less frequent and less efficient nucleokinesis with a net nuclear movement of 32.9 and 47.8 μm in *Kif21b*-depeted and control neurons, respectively (Figures 2M–2P). Defective nucleokinesis was further confirmed by shorter maximal distances between the nucleus and the centrosome, which is encompassed in the swelling, in neurons electroporated with sh-*Kif21b* #2 (Figures 2Q and 2R). We then investigated the dynamic branching of migrating neurons during active locomotion, excluding the phases of pausing. Although most control neurons persist bipolar during the locomotory phase with a single leading process that branched very transiently, *Kif21b*-depleted neurons, although still polarized, were characterized by multiple and heavily branched leading processes (Figure 2S). Overall, sh-*Kif21b* #2-expressing neurons showed an increased total branch length that arose from an increased number of shorter branches sprouting from either the soma or the leading process (Figures 2S–2V). As a result, neurons depleted for *Kif21b* spent statistically more time with multiple branches (Figure 2W), likely contributing, together with impaired nucleokinesis, to the decrease in migration velocity index observed in mutant projection neurons (Figure 2K). Collectively our data indicate that the kinesin Kif21b is critical to regulating neuronal polarization, nucleokinesis, and dynamic branching of projection neurons during glia-guided locomotion.

Kif21b motility on MTs is dispensable for its function in migrating projection neurons

Given the critical role of Kif21b in regulating intracellular transport in neurons,[26–29] we assessed whether Kif21b processive activity on MTs mediates Kif21b function in migrating neurons. First, we tested for restoration of the sh-*Kif21b* #2-induced phenotype by truncated Kif21b protein that lacks the motor domain (Kif21bΔMD; Figure 3A) by introducing full-length (FL) or Kif21bΔMD (NeuroD:Kif21b) together with inducible sh-*Kif21b* #2 and NeuroD:CRE in projection neurons using IUE at E14.5. Interestingly, Kif21b protein that lacks motor domain only partially rescued the distribution of *Kif21b*-depleted neurons with a significant number of neurons still trapped in the intermediate zone at E18.5 (Figures 3B and 3C), suggesting that this domain is partially required for Kif21b function in migrating neurons. To further test for the need of Kif21b motility

Figure 2. Kif21b depletion impedes glia-guided locomotion of projection neurons

(A) Drawing depicting the different steps of radial migration of projection neurons.

(B–W) Time-lapse imaging of neurons electroporated at E14.5 with NeuroD:Cre and NeuroD:IRES-GFP and either Cre-inducible shRNA *Kif21b* #2 or sh-scramble in E16.5 brain slices cultured for 1 day. (B) Locomotor paths (colored lines) of sh-scramble or sh-*Kif21b* #2 expressing neurons recorded for 10 h (h). Scale bar: 20 μm. (C) Time-lapse sequences of representative pyramidal neurons electroporated with the indicated constructs at E14.5. White and red arrowheads indicate, respectively, forward movement and pausing of the nucleus. Scale bar: 20 μm. (D) Percentage of GFP$^+$ neurons converting to a bipolar morphology or remaining as multipolar for 10-h recording. (E–K) Quantification (means ± SEM) of the percentage of GFP$^+$ bipolar neurons (BP) initiating locomotion (E), the mean velocity of locomotion (μm/h) (F), the total pause duration (min) (G), the average number of pauses per 10-h recording (H), the mean pause duration (min) (I), the percentage of neurons maintaining bipolar shape or converting to multipolar morphology (J), and the motility index (velocity without pauses [μm/h]) (K). (L) Schematic representation of the forward progression of pyramidal neurons during glia-guided locomotion. (M–P) Analysis (means ± SEM) of the average number of swelling (M) or nucleokinesis (N) during 10-h recording and mean amplitude (μm) (O) and duration (min) (P) of each nucleokinesis. (Q) Representative confocal images of migrating neurons after GFP immunolabeling (green) of E16.5 mouse cortices electroporated at E14.5 with NeuroD:Cre, NeuroD:GFP, and pCAGGS-PACT-mKO1 to label centrosome (CTR, red, arrowheads) and either Cre-inducible shRNA *Kif21b* #2 or sh-scramble. Nuclei were stained with DAPI (blue). Distances between nuclei and centrosome are indicated by a yellow line. Scale bar: 5 μm. (R) Quantification (means ± SEM) of the distance nucleus-centrosome (μm) in neurons extending a swelling in control and *Kif21b*-depleted cells. (S–W) Analysis (means ± SEM) of dynamic branching of the leading process showing branching types (S), number (T), mean length (μm) (U), total length (μm) (V) of branches, as well as time spent with multiple branches (min) (W).

Significance was calculated by unpaired t test, except in (S), where significance was calculated by two-way ANOVA. *$p < 0.05$, ***$p < 0.001$, ****$p < 0.0001$. Number of embryos analyzed: (D) $n \geq 6$; (J) $n \geq 7$. Number of cells analyzed from at least three embryos: (F–I and K) $n \geq 154$; (M and N) $n \geq 77$; (O and P) $n \geq 62$; (R) $n \geq 35$; and (S–W) $n \geq 71$.

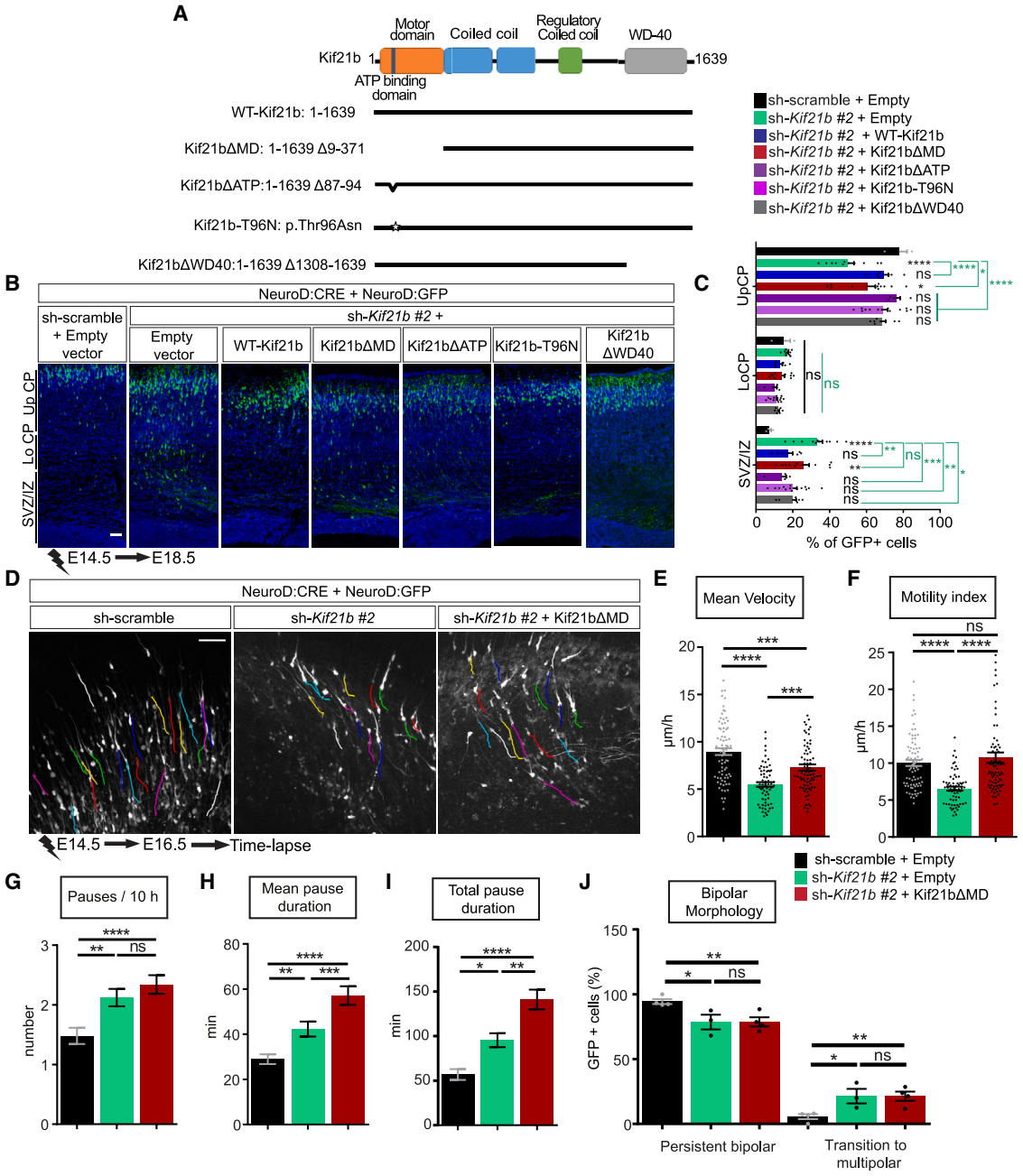

Figure 3. Kif21b motility on microtubules is not essential for its function in migrating projection neurons

(A) Different domains of the mouse Kif21b protein and the recombinants constructs used for the rescue experiments.

(B) Coronal sections of E18.5 mouse cortices electroporated at E14.5 with NeuroD:Cre and NeuroD:IRES-GFP together with shRNA in combination with NeuroD-constructs as indicated. GFP-positive electroporated cells are depicted in green. Nuclei are stained with DAPI. Scale bar, 50 µm.

(C) Histograms (means ± SEM) showing the distribution of GFP-positive neurons in different regions in all conditions as indicated. Number of embryos analyzed per condition: n ≥ 3. Significance was calculated by two-way ANOVA, Bonferroni's multiple comparisons test. *p < 0.05, **p < 0.005, ***p < 0.001, ****p < 0.0001.

(D–J) Time-lapse imaging of neurons electroporated at E14.5 with indicated constructs in E16.5 brain slices cultured for 1 day. (D) Locomotor paths (colored lines) of neurons expressing sh-scramble or sh-*Kif21b* #2 alone or in combination with NeuroD:Kif21bΔMD and recorded every 30 min for 10 h (h). Scale bar: 20 µm. (E–J) Analysis (means ± SEM) of the mean velocity (µm/h) (E), the velocity index (µm/h) (F), the average number of pauses per 10 h (G), the mean pause duration (min) (H), the total pause duration (min) (I), or the percentage of neurons converting to multipolar morphology (J).

Significance was calculated by two-way ANOVA, Bonferroni's multiple comparisons test. *p < 0.05, **p < 0.005, ***p < 0.001, ****p < 0.0001. Number of cells analyzed from at least three embryos: (E–I) n ≥ 66. Number of embryos analyzed: n ≥ 3 (J). See also Figure S3.

on MTs for neuronal migration, we performed complementation assays by expressing Kif21b protein that either cannot bind (NeuroD:Kif21bΔATP; Figure 3A) or hydrolyze ATP (NeuroD:Kif21b-T96N; Figure 3A)[27] in *Kif21b*-silenced neurons. Surprisingly, both constructs fully restored the migration phenotype at E18.5, demonstrating that motility of Kif21b is dispensable for its function during radial migration (Figures 3B and 3C). Accordingly, the carboxy-terminal (C-terminal) WD40 domain of Kif21b (Figure 3A), which is thought to promote interaction with cargoes,[24] is not essential for Kif21b migration-regulatory activities, because radial migration phenotype is fully rescued by overexpression of Kif21bΔWD40 construct (Figures 3B and 3C). Of note, Kif21b truncated or mutant proteins showed similar expression level in N2A neuroblastoma cell line, except for NeuroD:Kif21bΔATP, which tends to be lowly expressed (Figure S3A), and do not induce migration phenotypes while overexpressed under control conditions (sh-Scramble) (Figures S3B and S3C). We next sought to investigate the migration steps that are regulated by the motor domain of Kif21b. We performed time-lapse recording of brain organotypic slices after IUE of Kif21bΔMD construct together with inducible *Kif21b*-shRNA. In accordance with a partial rescue of *Kif21b*-silenced neurons distribution in the cortical plate, expression of Kif21b lacking the motor domain induced a rescue of 52.6% of the migration velocity of *Kif21b*-depleted neurons (Figures 3D and 3E). This partial rescue is likely due to the inability of Kif21bΔMD to restore pausing defects. Indeed, although Kif21bΔMD fully recovered the motility index phenotype (distance with respect to time minus pauses duration) (Figure 3F), it failed to restore the increased number of pauses (Figure 3G) and even induced more drastic defects on pauses duration (Figures 3H and 3I). In line with this, Kif21bΔMD expression did not rescue the loss of bipolar morphology of locomoting *Kif21b*-depeleted neurons (Figure 3J). Collectively, those data indicate that the N-terminal motor domain of Kif21b independently of its motility on MTs is critical to prevent pausing of cortical projection neurons during migration.

Kif21b regulates actin cytoskeletal dynamics through direct binding

We next sought to understand the function of Kif21b that mediates its roles during radial migration of projection neurons. First, to probe for candidate proteins that may interact with Kif21b, we performed Kif21b co-immunoprecipitation on E18.5 mouse cortices followed by mass spectrometry analysis. Among the 41 proteins identified (Table S1), 12 were proteins associated either to the MT cytoskeleton or, more unexpectedly, to the actin cytoskeleton (Figures 4A and S4A). Among those cytoskeleton candidates, we found several actin paralogues, actin-based motor proteins including components of the non-muscle myosin II (NM2) motor protein, that power actin contractile movement,[41] the unconventional myosin Va that transports cargoes along actin filaments,[42] and the actin-binding protein Drebrin (Dbn1). Given the predominant role of the actomyosin remodeling in neuronal cells[43–45] and the increasing evidence showing that disruption of actin cytoskeleton associates with neuronal migration defects in human,[9,22] the actin cytoskeleton emerged as a strong unlooked-for candidate to mediate Kif21b function in migrating neurons. To validate these interactions, we first performed anti-Kif21b immunoprecipitation assays on extracts from E18.5 WT cortices and confirmed the specific binding of Kif21b to both actin and myosin light chain 2 (MLC 2), a subunit of NM2 (Figures 4B and 4C). Reciprocal immunoprecipitation analysis using anti-actin antibody confirmed the specific interaction between Kif21b and actin (Figure 4B). Next, we purified actin from E18.5 cortices and detected Kif21b in the pellet containing polymerized filamentous actin (F-actin) (Figure 4D), further suggesting the ability of Kif21b to interact with filaments of actin. Corroborating these findings, Kif21b is enriched in the actin-rich growth cone fraction isolated from post-natal mouse cortices (Figure 4E). Immunolabeling of Kif21b, actin, and MTs in primary cortical neurons at DIV2 revealed localization of Kif21b both in axons and the central domain of the growth cone that are devoid of MTs and essentially composed of actin networks (Figure 4F). These data suggest that neuronal Kif21b likely interacts with actin cytoskeleton independently of its binding to MTs. To ascertain the localization of Kif21b on the actin cytoskeleton, we analyzed the relative localization of endogenous Kif21b and the actin cytoskeleton labeled with phalloidin using multicolor Single Molecule Localization Microscopy (SMLM) in primary cortical neurons at DIV2. STORM imaging revealed that Kif21b molecules organized as clusters localized along actin filaments following a spiral pattern in the growth cone, as well as in the neurites (Figure 4G). We performed quantitative analysis, based on the identification of objects from a Voronoi diagram,[46] of the shortest distance between the centroid of each Kif21b cluster and the actin lattice border. Computation of the distances indicated that most Kif21b clusters localized within 1.34 and 1.86 nm (median) from the actin filament (Figure 4H) in growth cone and neurites, respectively, demonstrating very close spatial approximation of Kif21b with actin filaments in cortical neurons. We next explored whether Kif21b directly binds to actin by performing *in vitro* co-sedimentation assays of pre-polymerized actin with purified recombinant Kif21b (Figure S4B; Table S2). Notably, although it contained negligible protein contaminants (Table S2), Kif21b purified fractions comprised FL His-tagged Kif21b, as well as shorter Kif21b fragments (Table S2). We detected FL Kif21b, as well as most of the short products, in the actin-enriched pellet (Figure 4I), suggesting a direct binding of Kif21b to polymerized actin. Accordingly, the same experiments in the absence of actin revealed that most Kif21b fragments were found in the supernatant. Finally, we investigated the roles of Kif21b on actin dynamics by recording, using spinning disc microscopy, dynamics of purified actin labeled with phalloidin and incubated with 1 nM recombinant Kif21b. Actin polymerization was enhanced in the presence of 1 nM Kif21b (Figure 4J), indicating that direct binding of Kif21b may favor the initial step of actin dynamics, meaning nucleation (Figure 4P). Notably, increasing the concentration of Kif21b to 10 nM had the reverse effect on actin nucleation (Figure S4C). We finally performed polymerization assays on beads coated or not with recombinant Kif21b protein and showed enhanced assembly of A488-phalloidin-labeled actin filaments on Kif21b-coated beads (Figures 4K and 4L) that further confirms Kif21b as a genuine actin nucleator. To

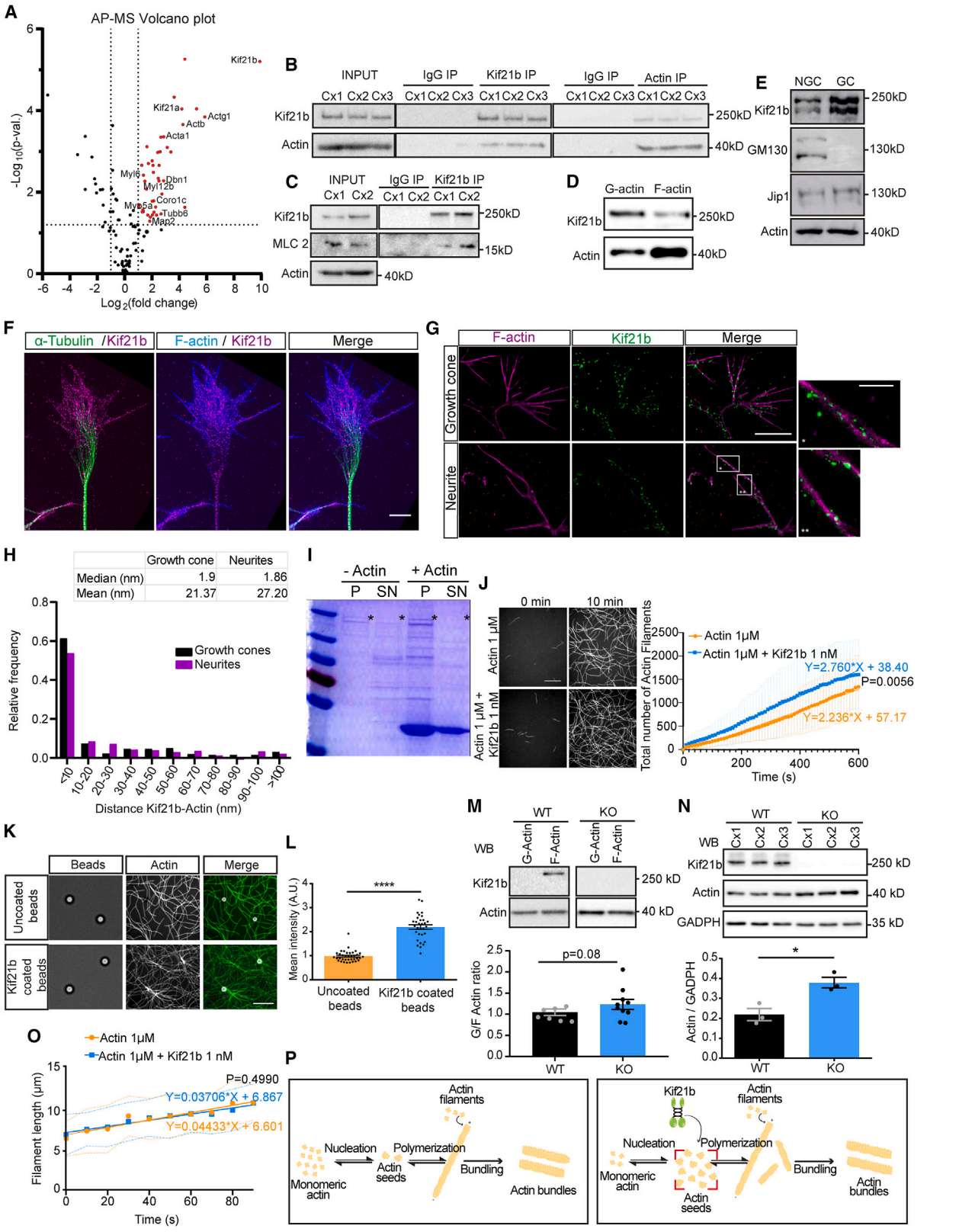

(legend on next page)

validate this actin-related function in cortices, we performed spinning disc analysis of dynamics of mouse embryonic brain actin labeled with phalloidin using protein extracts from E18.5 WT and KO (*Kif21b*$^{tm1a/tm1a}$) cortices. Corroborating assays with recombinant proteins, loss of *Kif21b* in embryonic cortices significantly limits *de novo* assembly of actin filaments as expected for a reduction of actin nucleation capacity (Figure S4D). Further analyses of the G/F actin ratio by ultracentrifugation sedimentation assay in E18.5 WT and *Kif21b* KO (*Kif21b*$^{tm1a/tm1a}$) cortices revealed that the proportion of the F-actin tends to decrease upon deletion of *Kif21b* compared with the control condition (Figure 4M), although measured total actin levels by western blot were increased in KO condition (Figure 4N). This confirms the positive role of Kif21b in regulating the nucleation of actin filaments in embryonic cortices (Figure 4P). Additional tracking of individual actin filament revealed that Kif21b did not affect filament elongation because similar rates of actin filament growth were measured in the presence of Kif21b and in actin-alone conditions (Figure 4O). Finally, to address whether Kif21b regulates bundling of actin filaments, we immobilized A488-phalloidin-labeled actin filaments on a glass surface and analyzed the ability of A568-actin filaments pre-incubated or not with 1 nM Kif21b to bundle with immobilized fragments (Figure S4E). The degree of co-localization between the two populations of actin (Pearson correlation coefficient) and the fraction of actin bundles was low and independent of the presence of Kif21b, indicating that Kif21b is unlikely to be an actin bundler (Figures S4F–S4H). Altogether, these data converged toward a direct role of Kif21b in regulation of actin dynamics (Figure 4P).

Kif21b depletion leads to aberrant actin dynamics in migrating neurons

Although well studied in the context of tangential migration of interneurons[47,48] or glia-guided migration of cerebellar granular neurons,[43] the actin cytoskeletal dynamics in migrating cortical projection neurons has been poorly addressed. We first examined the spatial distribution of actin during glia-guided locomotion of cortical projection neurons in brain organotypic slices after IUE of LifeAct-Ruby[49] or Utroph-GFP,[50] two probes that label F-actin, in E14.5 cortices. Time-lapse imaging in control neurons (sh-Scramble) revealed that both LifeAct-labeled F-actin (Figures 5A and 5B) and Utroph-GFP (Figures S5A and S5B) accumulated in the proximal part of the leading process before the translocation of the nucleus and dropped severely once the nuclear movement is completed. Interestingly, although actin dynamics were similar in control and *Kif21b*-depleted neurons before nucleokinesis, F-actin accumulation in the leading process persisted after the forward movement of the nucleus in neurons electroporated with sh-*Kif21b* #2 (Figures 5A and 5C). These data demonstrated the critical role of Kif21b in regulating actin dynamics *in vivo* in migrating neurons. Given the predominant role of actomyosin contraction in promoting nuclear translocation of migrating neurons[43–45] and the binding of Kif21b to NM2 (Figures 4B and 4C), we tested the ability of para-amino-Blebbistatin, which inhibits actomyosin contraction through inhibition of Myosin II motor activity, to rescue the dynamics of migrating neurons. Organotypic slices of brains electroporated with inducible sh-*Kif21b* #2 or sh-scramble, NeuroD:CRE, and NeuroD:GFP were recorded for 5 h, then

Figure 4. Kif21b regulates actin cytoskeletal dynamics through direct binding

(A) Affinity purification-mass spectrometry (AP-MS) results showing, in red, proteins that are specifically interacting with Kif21b in E18.5 mouse cortices.

(B and C) Western blot analysis of Kif21b or actin immunoprecipitation (IP) experiments in three independent E18.5 mouse cortices (Cx 1–3) showing reciprocal interaction between Kif21b and actin (B) and binding of myosin light chain 2 (MLC2) to Kif21b (C). Whole-cortex extracts are shown as input.

(D) Western blot F-actin sedimentation assay from E18.5 wild-type (WT) mouse cortices.

(E) Growth cone fractionation assay showing growth cone (GC, enriched for vesicle marker Jip1) and a non-growth cone fraction (NGC, enriched for Golgi marker GM130) isolated from P2 WT mouse cortices.

(F) Triple staining of Kif21b (red), α-tubulin (green), and F-actin (phalloidin, in blue) in a growth cone of a DIV2 neuron imaged by confocal microscopy. Scale bar: 5 μm.

(G) Single Molecule Localization Microscopy (SMLM) showing Kif21b (green) and F-actin (phalloidin, red) double staining in a growth cone and a neurite of a DIV2 neuron. Scale bar: 5 μm. Insets are shown by one (*) or two asterisks (**). Scale bar in insets, 1 μm.

(H) Analysis of the distribution probability of the distance (nm) between Kif21b clusters and actin filaments in both growth cones and neurites. Growth cones, n = 259 particles analyzed from 3 neurons; neurites, n = 331 particles analyzed from four neurons; experiment was done in two independent replicates.

(I) *In vitro* co-sedimentation assay of recombinant Kif21b in the presence or absence of actin, showing that full-length Kif21b (asterisk) and shorter fragments co-sediment with polymerized actin found in the pellet (P).

(J) Representative spinning-disk images of *in vitro* analysis of actin polymerization dynamics (stained with phalloidin) at the beginning (0′) and at end (10′) of the experiment in the presence or absence of recombinant Kif21b (1 nM). Scale bar, 10 μm. The graph shows the number of actin filaments assembled during a 600-s time lapse. Significance was calculated by linear regression to determine differences in curves for each dataset. Number of replicates: n $\geq$ 6 in three different experiments.

(K) Representative images of actin filaments after 10 min of polymerization in the presence of beads coated or not with recombinant Kif21b.

(L) Quantification of the mean intensity of polymerized actin on the beads. Significance was calculated by unpaired t test, ****p < 0.0005. Number of beads measured: n $\geq$ 31.

(M) Quantitative analysis (mean ± SEM) of western blot of actin sedimentation assay performed in E18.5 WT and *Kif21b*$^{Tm1a/Tm1a}$ (KO) mouse cortices.

(N) Western blot analysis of total actin levels in three independent E18.5 WT and *Kif21b*$^{Tm1a/Tm1a}$ (KO) mouse cortices (Cx 1–3) showing (means ± SEM) increased actin level in KO samples. (M and N) Significance was calculated by unpaired t test, *p < 0.05. Number of embryos analyzed: (M) n $\geq$ 7; (N) n = 3.

(O) *In vitro* actin polymerization in the absence or presence of recombinant Kif21b (1 nM) analyzed as the length of individual filaments of actin during an 80-s time lapse. Significance was calculated by linear regression to determine differences in curves for each dataset. Number of filaments analyzed: n $\geq$ 12 in three different experiments.

(P) Scheme representing the positive effect of Kif21b on actin nucleation without affecting polymerization or bundling.

SN, supernatant. See also Figure S4.

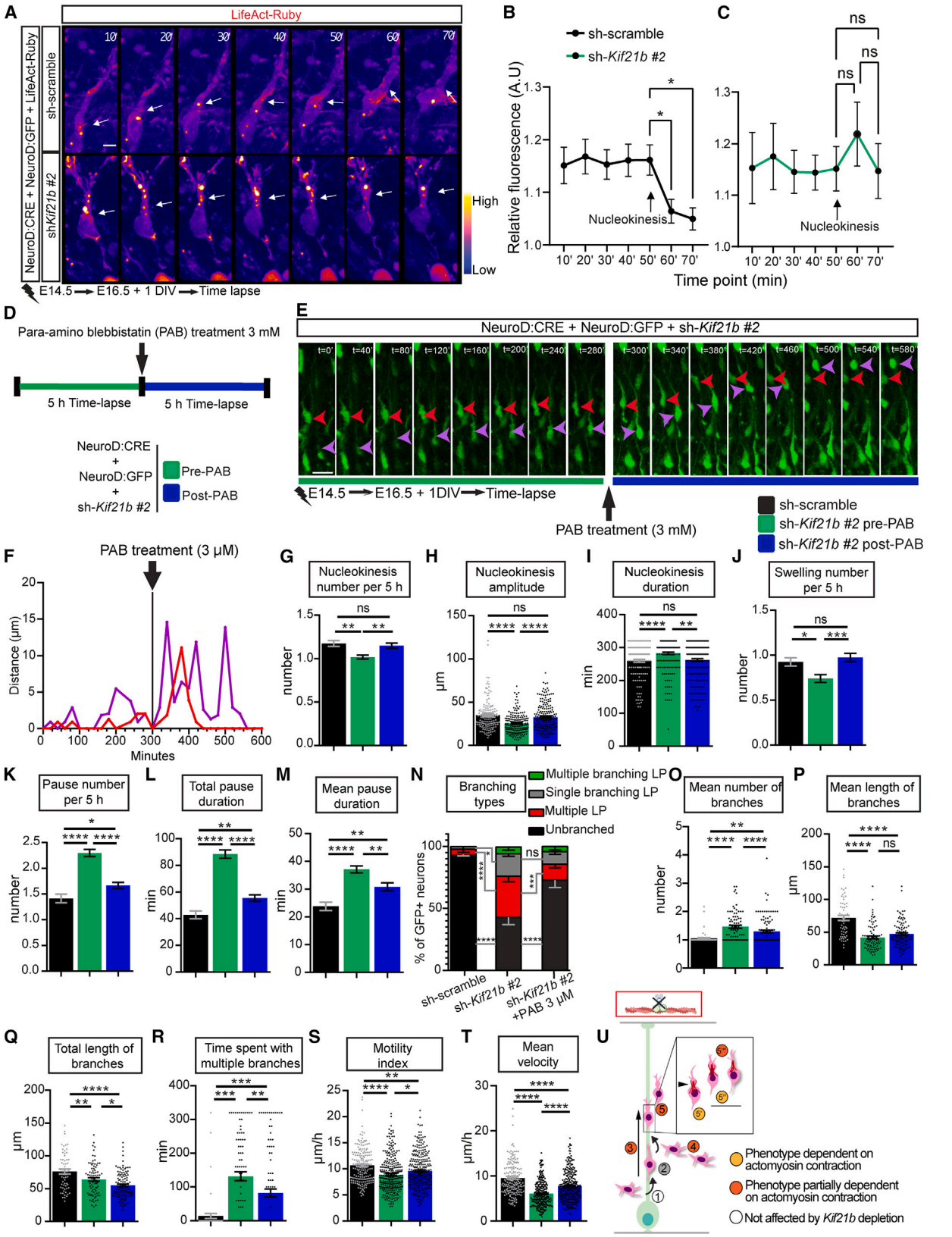

(legend on next page)

treated with para-amino-Blebbistatin at 3 μM and imaged for an additional 5 h (Figures 5D–5F). Alteration of most of the migration parameters in sh-scramble neurons treated with para-amino-Blebbistatin confirmed the efficiency of the treatment (Figures S5C–S5G). Defects in nucleokinesis and swelling formation observed upon *Kif21b* depletion were fully rescued after para-amino-Blebbistatin treatment (Figures 5G–5J), suggesting that faulty nucleokinesis induced by *Kif21b* depletion relies on elevated myosin activity and actomyosin contraction. Because we demonstrated that Kif21b regulates migration pausing independently of its motility on MTs (Figures 3G–3I), we tested whether pausing could be related to actin-dependent Kif21b function. We showed a partial rescue of the number (Figure 5K) and the duration of pauses (Figures 5L and 5M) of *Kif21b*-depleted locomoting neurons upon para-amino-Blebbistatin, suggesting that defects in pausing depend, at least partly, on the modulation of actomyosin contractility. Finally, we showed that inhibition of Myosin II motor activity with para-amino-Blebbistatin partially restored the branching defects observed in *Kif21b*-depleted neurons (Figures 5N–5R), except for the mean length of branches that is similar before and after para-amino-Blebbistatin treatment (Figure 5P), suggesting that actomyosin-dependent mechanisms contribute to the Kif21b-dependent regulation of the dynamic branching of the leading process. Overall, the full rescue of nucleokinesis and the partial rescue of pausing and multiple branches upon para-amino-Blebbistatin treatment greatly improved the radial migration of *Kif21b*-depeleted projection neurons by increasing both the motility index and the mean velocity (9.5 μm/h in control condition, 6.1 μm/h sh-*Kif21b* #2 pre-para-amino-Blebbistatin, 7.7 μm/h sh-*Kif21b* #2 post-para-amino-Blebbistatin) (Figures 5F, 5S, and 5T). Collectively, these results showed that Kif21b is required to fine-tune actin dynamics during specific steps of glia-guided locomotion, including nucleokinesis, pausing, and branching of the leading process (Figure 5U).

DISCUSSION

Our findings uncover physiological roles for Kif21b during radial migration of projection neurons. Although it is dispensable for the newborn pyramidal neurons to reach the intermediate zone and convert to a bipolar shape, Kif21b paces the glia-guided locomotion by controlling nucleokinesis, dynamic branching, and pausing of migrating neurons. To date, several members of the kinesin superfamily have been shown to play critical functions during radial migration.[51–61] Yet, unlike Kif21b, many of them regulate the initial multipolar-to-bipolar transition.[51,55,56,59–61] Noteworthy, dynamic analysis of each stage of migration (multipolar-to-bipolar transition or bipolar locomotion) has not been performed systematically, preventing the exact delineation of the functions of those kinesins during radial migration.

Our study unravels the molecular mechanisms underlying Kif21b functions in migrating neurons. Several lines of evidence suggest that Kif21b regulates different phases of migration through distinct functional domains. First, our complementation experiments revealed that (1) although the N-terminal motor domain is partially required for Kif21b to promote neuronal migration, its ability to hydrolyze or bind ATP is nonessential; and (2) the C-terminal WD40 repeat (WDR) domain that likely binds cargoes[24] is not necessary to promote migration. This demonstrates that the N-terminal domain, independently of its motility, and the coiled-coil central region are both necessary but, individually, not sufficient for Kif21b functions in pyramidal neurons during migration. Second, rescue analysis with the truncated Kif21bΔMD protein showed that the N-terminal domain is dispensable for the processivity of locomoting neurons but necessary to maintain the bipolar morphology and to limit pausing during locomotion. It suggests that the N-terminal domain and the coiled-coil domain ensure the functions of Kif21b in neuronal polarization and active locomotion, respectively. Because the N-terminal domain is essential for the inhibition of MT growth,[30,32] it is tempting to postulate that Kif21b

Figure 5. *Kif21b* depletion leads to aberrant actin dynamics in migrating neurons

(A) Representative sequence of migrating pyramidal neurons recorded during 5 h in E16.5 organotypic slices electroporated at E14.5 with NeuroD:Cre, NeuroD:IRES-GFP, and pCAGGS-LifeAct-Ruby together with Cre-inducible shRNA *Kif21b #2* or sh-scramble and cultured for 1 day. Intensity of the LifeAct-Ruby is shown by ImageJ fire look-up table. Scale bar: 10 μm. Arrows point toward the proximal part of the leading process where actin accumulation severely dropped after nucleokinesis in control condition.

(B and C) Quantification of the relative LifeAct-Ruby fluorescence (A.U.) at the proximal part of the leading process in the LifeAct-Ruby$^+$ control (B) or *Kif21b*-depleted neurons (C) before and after nucleokinesis (indicated by an arrow). Data were analyzed by fitting a mixed-model, Tukey's multiple comparisons test. *$p < 0.05$. Number of cells analyzed: $n \geq 22$.

(D) Schematic representation of the rescue experimental approach with para-amino-Blebbistatin (PAB).

(E) Representative images of *Kif21b*-silenced neurons during a time-lapse experiment before and after PAB 3 μM treatment. Red and purple arrowheads indicate two neurons localization during the whole time lapse. Scale bar: 20 μm.

(F) Graph showing the net movement (μm) between two time points (20 min) of two representative migrating neurons depicted in red and purple in (E), before and after PAB treatment (arrow).

(G–M) Analysis (mean ± SEM) of the frequency (G), amplitude (μm) (H), and duration (min) (I) of nucleokinesis, as well as the swelling frequency (J) of the migrating neurons in a 5-h time lapse, the pause number (K), total pauses duration (min) (L), and mean pauses duration (min) (M) pre- and post-PAB treatment.

(N–R) Quantification (means ± SEM) of branching types (N), number (O), mean length of branches (μm) (P), total branching length (μm) (Q), and time spent with multiple branches (R).

(S and T) Motility index (μm/h) (S) and mean velocity (μm/h) (T) of migrating neurons measured in organotypic slices (means ± SEM).

(U) Summary scheme illustrating the steps of migration that are regulated by Kif21b and that depend fully (light orange) or partially (dark orange) on Kif21b regulatory function on actomyosin contraction. Actin filaments are represented in red.

Significance was calculated by one-way ANOVA, except in (N), where significance was calculated by two-way ANOVA. *$p < 0.05$, **$p < 0.01$, ***$p < 0.001$, ****$p < 0.0001$. Number of neurons analyzed from at least three embryos: (G–J) $n \geq 124$; (K–O and S–T) $n \geq 177$; (P–R) $n \geq 60$. See also Figure S5.

maintains bipolar morphology through the regulation of MT polymerization. Indeed, neuronal polarization largely relies on remodeling of the MT cytoskeleton[62,63] and stabilization of MTs instructs neuronal polarization.[64,65] Overgrowth of MTs induced by loss of Kif21b[27,30,33] could therefore compromise the bipolarity of locomoting neurons. Such a hypothesis should be further tested by examining the ability of MT-depolymerizing drugs, such as vinblastine, to rescue bipolar morphology of *Kif21b*-depleted migrating neurons.[33] In line with an MT-dependent effect, we showed that para-amino-Blebbistatin treatment partially rescued the faulty pausing observed upon *Kif21b* knockdown, suggesting that the role of Kif21b in pausing does not fully rely on the regulation of the actomyosin network. In addition, because the N-terminal region of Kif21b binds to the unconventional Myosin Va in a neuronal-activity-dependent manner,[66] one cannot exclude that Kif21b cooperates with Myosin Va to regulate actin dynamics in bipolar neurons, although, to date, neuronal activity has been shown to facilitate the initial step of projection neurons migration, the multipolar-to-bipolar conversion, unlikely regulated by Kif21b (Figure 2).[67] The central coiled-coil domain contains a secondary MT-binding domain that promotes MT assembly and limits catastrophe frequency, although it is unclear whether it could act alone or exclusively in combination with the other secondary MT-binding domain within the WD40 tail.[26,29,30] Further work is required to delineate the function of each MT-binding domain in migrating neurons. Third, our *in vitro* co-sedimentation assays of pre-polymerized actin with purified recombinant Kif21b revealed short fragments of Kif21b that might specifically bind to actin. Interestingly, those Kif21b fragments encompass all the functional domains of Kif21b, suggesting that Kif21b binds actin through multiple domains, including its central region. Accordingly, our attempts to precisely map Kif21b actin-binding domain(s) using immunoprecipitation of various Kif21b truncated proteins that either lack or only encompass the motor domain, regulatory coiled-coil domain (rCC), coil-coiled domain 1 or 2, or WD40 region were inconsistent and suggest that Kif21b binding to actin filaments requires specific structural conformation involving distinct and potentially distant protein domains. To date, our knowledge about the precise domains of binding to MT, actin or Myosins is limited, with only large domains identified.[26,29,30,66] In addition, the high overlap between those domains raises the possibility of competitive binding of Kif21b to actin and MT networks.

Our data provide the evidence for a direct role of a kinesin on actin cytoskeleton in mammals. Indeed, to date, only a plant- and a *Dictyostelium*-specific kinesin[68,69] were shown to bind actin. Here, we first ascertained a direct binding of Kif21b to actin filaments by super-resolution imaging of cortical neurons in culture and by co-sedimentation assay with purified recombinant proteins (Figure 4). This validates previous proteomic data suggesting binding of actin and actin-binding partners to exogenous Kif21b purified from HEK-293T cells.[26] Then, investigations of the role of Kif21b on actin dynamics revealed that Kif21b favors the initial step of actin polymerization, the nucleation, but not the subsequent elongation or bundling of actin filaments, suggesting that Kif21b facilitates the formation of actin seeds but does not regulate, at least through direct interaction, the elongation and crosslinking of actin filaments once formed. Very interestingly, the effect of Kif21b on actin assembly highly depends on the stoichiometric ratio between actin and Kif21b molecules (Figures 4 and S4). This is reminiscent of the effect of Kif21b on the dynamics of the MT cytoskeleton in cells, with high and low kinesin concentrations leading to opposite effects on MT growth and stability.[26,29,30] Altogether, these findings indicate that Kif21b might regulate all steps of actin network dynamics through either direct (nucleation) or indirect (elongation and branching) mechanisms.

At the cellular level, except for the Kinesin 6 that has been shown to perturb actin localization during the initial multipolar-to-bipolar transition through unknown mechanisms,[55] very little is known about kinesin and actin interplay in migrating cortical projection neurons. Here we showed, in control neurons, that F-actin accumulates ahead of the nucleus before nucleokinesis, in line with previous observations in both cortical projection neurons[16] and in the cerebellar granule neurons that also undergo glia-guided locomotion.[43] Reminiscent of what has been shown in cerebellar neurons, in which a retrograde actin flow away from the proximal region of the leading process drives nucleokinesis,[43] actin concentration at the front of the nucleus drastically drops in cortical projection neurons after nuclear movement. Interestingly, this dynamic actin turnover does not occur in migrating cortical neurons lacking Kif21b, suggesting that Kif21b controls nucleokinesis by controlling actin remodeling. Because NM2 activity ahead of the nucleus is critical for nucleokinesis,[43,45] we hypothesized that Kif21b, through its binding to both actin and NM2, might regulate actomyosin contraction during nuclear forward movement. Our rescue experiments using para-amino-Blebbistatin indicate that the faulty nucleokinesis induced by the depletion of *Kif21b* fully depends on the perturbation of NM2 activity (Figure 5). This further suggests that the high concentration of F-actin observed, after nucleokinesis, in the proximal leading process upon *Kif21b* depletion is caused by a defect in the retrograde actin flow, which is thought to be NM2 dependent.[43] Finally, we showed that Kif21b likely regulates pausing and the dynamic branching of the leading process, at least partly, through regulation of actomyosin contraction. Collectively, these results indicate that Kif21b promotes glia-guided locomotion of projection neurons by regulating nucleokinesis, pausing, and dynamic branching though non-canonical functions on the actin cytoskeleton.

In conclusion, our results indicate that Kif21b plays pleiotropic functions during all steps of the glia-guided locomotion of cortical projection neurons. These cellular functions, driven by distinct protein domains, are independent of the canonical processivity of Kif21b and likely rely on regulation of both MTs and actin cytoskeletons dynamics. As it has been suggested for the plant-specific kinesin GhKCH1[69] and the *Dictyostelium*-specific kinesin DdKin5,[68] our work opens the question of the roles of Kif21b in the interplay between MTs and actin during neuronal migration. Interestingly, our interatomic study revealed, among the main binding partners of Kif21b, the Drebrin protein, which directly associates and connects MT and actin cytoskeletons in maturing neurons.[70,71] One can speculate that Drebrin could mediate some of the functions of Kif21b likely by regulating the interface of neuronal MTs and actin networks in migrating neurons. Overall, this would add an atypical function of kinesins in

the coordination of actin and MT networks during mammalian brain development.

Limitations of the study

Our study suggested that dual functions of Kif21b in both MTs and actin cytoskeletons are required to regulate the glia-guided locomotion of projection neurons. Although we demonstrated that acto-myosin-dependent mechanisms are at play during nucleokinesis, our results also indicated that additional mechanisms, likely involving direct regulation of actin dynamics or MT growth, contribute to the function of Kif21b during pausing and dynamic branching. In our experimental setup, the sensitivity of the LifeAct or Utroph-GFP was not compatible with analysis of actin dynamics during branching and pausing, limiting analysis of the consequences of *Kif21b* depletion on neuronal polarization. Likewise, our analyses were designed to address actin- and MT-related mechanisms independently, restraining the understanding of potential crosstalk between both cytoskeletons. Because we were not able to precisely map Kif21b actin-binding domain(s), refinement of the domains through structural analysis of Kif21b either bound to actin or MT would be needed to understand the cooperative or competitive function(s) of Kif21b on both actin and MT cytoskeletons. In addition, further rescue analysis with truncated Kif21b constructs lacking actin-binding domain(s), if not overlapping with MT-binding domains, or drugs that alter MT or actin dynamics alone or in combination, would help better delineate actin- versus MT-dependent function(s) of Kif21b during neuronal migration.

STAR★METHODS

Detailed methods are provided in the online version of this paper and include the following:

SUPPLEMENTAL INFORMATION

Supplemental information can be found online at https://doi.org/10.1016/j.celrep.2023.112744.

ACKNOWLEDGMENTS

This work was supported by grants from INSERM (ATIP-Avenir program, J.D.G.), the Fyssen Foundation (J.D.G.), the French state funds through the Agence Nationale de la Recherche (JCJC CREDO ANR-14-CE13-0008-01 to J.D.G.; ANR-10-IDEX-0002-02 and ANR-10-LABX-0030-INRT to J.D.G., A.-C.R., and M.R.; SFRI-STRAT'US project [ANR 20-SFRI-0012]; and EUR IMCBio [ANR-17-EURE-0023]), INSERM/CNRS, and University of Strasbourg. L.A. and J.R.A. were supported through the IGBMC PhD program and Fondation pour la recherche médicale. R.B. was supported by an ANR JCJC grant (ANR-19-CE13-0005-01 to A.-C.R.). P.T. and J.B. are, respectively, research assistant and assistant professor at the University of Strasbourg. C.B. was supported by CERBM-GIE. L.R. and B.M. are research engineers at CNRS. F.L. is a research engineer at INSERM. J.D.G. is an INSERM investigator. Y.M. is professor at the University of Strasbourg and Institut Universitaire de France. A.-C.R. is a CRNS investigator. We thank the Imaging Center of IGBMC (https://ici.igbmc.fr/), in particular Elvire Guiot and Erwan Grandgirard, for their assistance in the imaging experiments. We are grateful to the staff of the mouse facilities of the Institut Clinique de la souris (ICS) and IGBMC, of the proteomics platform, and of the molecular biology service (in particular, Thierry Lerouge and Paola Rossolillo) for their involvement in the project. The SMLM imaging was supported by the Imaging Center PIQ-QuESt (https://piq.unistra.fr). We warmly thank Dr. Binnaz Yalcin, Dr. Laurent Blanchoin, and Christophe Guérin for helpful comments, advice, and reagents. We are also grateful to members of J.D.G.'s laboratory for discussion and technical assistance and to Sandra Bour for her help preparing the graphical abstract.

AUTHOR CONTRIBUTIONS

J.R.A. and L.A. conceived and designed the experiments, performed the experiments, performed statistical analysis, and analyzed the data related to cellular and functional studies in mice. P.T. performed IUE. P.T. and N.S. provided technical assistance. R.B. and A.-C.R. conceived, designed, and performed *in vitro* actin experiments. C.B., J.B., and M.R. contributed to the production of recombinant Kif21b proteins. B.M. performed mass spectrometry analysis and analyzed data. L.R. performed SMLM acquisition and performed quantitative analysis using a plugin developed by F.L. Y.M. contributed to SMLM data analysis and interpretation. J.D.G. conceived, coordinated, and supervised the study; designed experiments; analyzed data; and wrote the manuscript.

DECLARATION OF INTERESTS

The authors declare no competing interests.

Received: December 13, 2022
Revised: May 18, 2023
Accepted: June 19, 2023
Published: July 6, 2023

REFERENCES

1. Greig, L.C., Woodworth, M.B., Galazo, M.J., Padmanabhan, H., and Macklis, J.D. (2013). Molecular logic of neocortical projection neuron specification, development and diversity. Nat. Rev. Neurosci. *14*, 755–769. https://doi.org/10.1038/nrn3586.

2. Jabaudon, D. (2017). Fate and freedom in developing neocortical circuits. Nat. Commun. *8*, 16042. https://doi.org/10.1038/ncomms16042.

3. Rash, B.G., and Grove, E.A. (2006). Area and layer patterning in the developing cerebral cortex. Curr. Opin. Neurobiol. *16*, 25–34. https://doi.org/10.1016/j.conb.2006.01.004.

4. Molyneaux, B.J., Arlotta, P., Menezes, J.R.L., and Macklis, J.D. (2007). Neuronal subtype specification in the cerebral cortex. Nat. Rev. Neurosci. *8*, 427–437. https://doi.org/10.1038/nrn2151.

5. Wonders, C.P., and Anderson, S.A. (2006). The origin and specification of cortical interneurons. Nat. Rev. Neurosci. *7*, 687–696. https://doi.org/10.1038/nrn1954.

6. Barkovich, A.J., Guerrini, R., Kuzniecky, R.I., Jackson, G.D., and Dobyns, W.B. (2012). A developmental and genetic classification for malformations of cortical development: update 2012. Brain *135*, 1348–1369. https://doi.org/10.1093/brain/aws019.

7. Fernández, V., Llinares-Benadero, C., and Borrell, V. (2016). Cerebral cortex expansion and folding: what have we learned? EMBO J. *35*, 1021–1044. https://doi.org/10.15252/embj.201593701.

8. Guerrini, R., and Dobyns, W.B. (2014). Malformations of cortical development: clinical features and genetic causes. Lancet Neurol. *13*, 710–726. https://doi.org/10.1016/S1474-4422(14)70040-7.

9. Francis, F., and Cappello, S. (2021). Neuronal migration and disorders - an update. Curr. Opin. Neurobiol. *66*, 57–68. https://doi.org/10.1016/j.conb.2020.10.002.

10. Nadarajah, B., Brunstrom, J.E., Grutzendler, J., Wong, R.O., and Pearlman, A.L. (2001). Two modes of radial migration in early development of the cerebral cortex. Nat. Neurosci. *4*, 143–150. https://doi.org/10.1038/83967.

11. Noctor, S.C., Martínez-Cerdeño, V., Ivic, L., and Kriegstein, A.R. (2004). Cortical neurons arise in symmetric and asymmetric division zones and migrate through specific phases. Nat. Neurosci. *7*, 136–144. https://doi.org/10.1038/nn1172.

12. LoTurco, J.J., and Bai, J. (2006). The multipolar stage and disruptions in neuronal migration. Trends Neurosci. *29*, 407–413. https://doi.org/10.1016/j.tins.2006.05.006.

13. Tabata, H., and Nakajima, K. (2003). Multipolar migration: the third mode of radial neuronal migration in the developing cerebral cortex. J. Neurosci. *23*, 9996–10001.

14. Tanaka, T., Serneo, F.F., Higgins, C., Gambello, M.J., Wynshaw-Boris, A., and Gleeson, J.G. (2004). Lis1 and doublecortin function with dynein to mediate coupling of the nucleus to the centrosome in neuronal migration. J. Cell Biol. *165*, 709–721. https://doi.org/10.1083/jcb.200309025.

15. Tanaka, T., Serneo, F.F., Tseng, H.C., Kulkarni, A.B., Tsai, L.H., and Gleeson, J.G. (2004). Cdk5 phosphorylation of doublecortin ser297 regulates its effect on neuronal migration. Neuron *41*, 215–227. https://doi.org/10.1016/s0896-6273(03)00852-3.

16. Martinez-Garay, I., Gil-Sanz, C., Franco, S.J., Espinosa, A., Molnár, Z., and Mueller, U. (2016). Cadherin 2/4 signaling via PTP1B and catenins is crucial for nucleokinesis during radial neuronal migration in the neocortex. Development *143*, 2121–2134. https://doi.org/10.1242/dev.132456.

17. Hurni, N., Kolodziejczak, M., Tomasello, U., Badia, J., Jacobshagen, M., Prados, J., and Dayer, A. (2017). Transient Cell-intrinsic Activity Regulates the Migration and Laminar Positioning of Cortical Projection Neurons. Cerebr. Cortex *27*, 3052–3063. https://doi.org/10.1093/cercor/bhx059.

18. Liaci, C., Camera, M., Caslini, G., Rando, S., Contino, S., Romano, V., and Merlo, G.R. (2021). Neuronal Cytoskeleton in Intellectual Disability: From Systems Biology and Modeling to Therapeutic Opportunities. Int. J. Mol. Sci. *22*, 6167. https://doi.org/10.3390/ijms22116167.

19. Lian, G., and Sheen, V.L. (2015). Cytoskeletal proteins in cortical development and disease: actin associated proteins in periventricular heterotopia. Front. Cell. Neurosci. *9*, 99. https://doi.org/10.3389/fncel.2015.00099.

20. Moon, H.M., and Wynshaw-Boris, A. (2013). Cytoskeleton in Action: Lissencephaly, a Neuronal Migration Disorder, *2* (Wiley Interdiscip Rev Dev Biol), pp. 229–245. https://doi.org/10.1002/wdev.67.

21. Wu, Q., Liu, J., Fang, A., Li, R., Bai, Y., Kriegstein, A.R., and Wang, X. (2014). The dynamics of neuronal migration. Adv. Exp. Med. Biol. *800*, 25–36. https://doi.org/10.1007/978-94-007-7687-6_2.

22. Stouffer, M.A., Golden, J.A., and Francis, F. (2016). Neuronal migration disorders: Focus on the cytoskeleton and epilepsy. Neurobiol. Dis. *92*, 18–45. https://doi.org/10.1016/j.nbd.2015.08.003.

23. Labonté, D., Thies, E., and Kneussel, M. (2014). The kinesin KIF21B participates in the cell surface delivery of gamma2 subunit-containing GABAA receptors. Eur. J. Cell Biol. *93*, 338–346. https://doi.org/10.1016/j.ejcb.2014.07.007.

24. Marszalek, J.R., Weiner, J.A., Farlow, S.J., Chun, J., and Goldstein, L.S. (1999). Novel dendritic kinesin sorting identified by different process targeting of two related kinesins: KIF21A and KIF21B. J. Cell Biol. *145*, 469–479.

25. Asselin, L., Rivera Alvarez, J., Heide, S., Bonnet, C.S., Tilly, P., Vitet, H., Weber, C., Bacino, C.A., Baranaño, K., Chassevent, A., et al. (2020). Mutations in the KIF21B kinesin gene cause neurodevelopmental disorders through imbalanced canonical motor activity. Nat. Commun. *11*, 2441. https://doi.org/10.1038/s41467-020-16294-6.

26. van Riel, W.E., Rai, A., Bianchi, S., Katrukha, E.A., Liu, Q., Heck, A.J., Hoogenraad, C.C., Steinmetz, M.O., Kapitein, L.C., and Akhmanova, A. (2017). Kinesin-4 KIF21B is a potent microtubule pausing factor. Elife *6*, e24746. https://doi.org/10.7554/eLife.24746.

27. Muhia, M., Thies, E., Labonté, D., Ghiretti, A.E., Gromova, K.V., Xompero, F., Lappe-Siefke, C., Hermans-Borgmeyer, I., Kuhl, D., Schweizer, M., et al. (2016). The Kinesin KIF21B Regulates Microtubule Dynamics and Is Essential for Neuronal Morphology, Synapse Function, and Learning and Memory. Cell Rep. *15*, 968–977. https://doi.org/10.1016/j.celrep.2016.03.086.

28. Gromova, K.V., Muhia, M., Rothammer, N., Gee, C.E., Thies, E., Schaefer, I., Kress, S., Kilimann, M.W., Shevchuk, O., Oertner, T.G., and Kneussel, M. (2018). Neurobeachin and the Kinesin KIF21B Are Critical for Endocytic Recycling of NMDA Receptors and Regulate Social Behavior. Cell Rep. *23*, 2705–2717. https://doi.org/10.1016/j.celrep.2018.04.112.

29. Ghiretti, A.E., Thies, E., Tokito, M.K., Lin, T., Ostap, E.M., Kneussel, M., and Holzbaur, E.L.F. (2016). Activity-Dependent Regulation of Distinct Transport and Cytoskeletal Remodeling Functions of the Dendritic Kinesin KIF21B. Neuron *92*, 857–872. https://doi.org/10.1016/j.neuron.2016.10.003.

30. Masucci, E.M., Relich, P.K., Lakadamyali, M., Ostap, E.M., and Holzbaur, E.L.F. (2022). Microtubule dynamics influence the retrograde biased motility of kinesin-4 motor teams in neuronal dendrites. Mol. Biol. Cell *33*, ar52. https://doi.org/10.1091/mbc.E21-10-0480.

31. Ganchala, D., Pinto-Benito, D., Baides, E., Ruiz-Palmero, I., Grassi, D., and Arevalo, M.A. (2023). Kif21B mediates the effect of estradiol on the morphological plasticity of mouse hippocampal neurons. Front. Mol. Neurosci. *16*, 1143024. https://doi.org/10.3389/fnmol.2023.1143024.

32. Taguchi, S., Nakano, J., Imasaki, T., Kita, T., Saijo-Hamano, Y., Sakai, N., Shigematsu, H., Okuma, H., Shimizu, T., Nitta, E., et al. (2022). Structural model of microtubule dynamics inhibition by kinesin-4 from the crystal structure of KLP-12 -tubulin complex. Elife *11*, e77877. https://doi.org/10.7554/eLife.77877.

33. Hooikaas, P.J., Damstra, H.G., Gros, O.J., van Riel, W.E., Martin, M., Smits, Y.T., van Loosdregt, J., Kapitein, L.C., Berger, F., and Akhmanova, A. (2020). Kinesin-4 KIF21B limits microtubule growth to allow rapid centrosome polarization in T cells. Elife *9*, e62876. https://doi.org/10.7554/eLife.62876.

34. Huang, C.F., and Banker, G. (2012). The translocation selectivity of the kinesins that mediate neuronal organelle transport. Traffic *13*, 549–564. https://doi.org/10.1111/j.1600-0854.2011.01325.x.

35. Kannan, M., Bayam, E., Wagner, C., Rinaldi, B., Kretz, P.F., Tilly, P., Roos, M., McGillewie, L., Bär, S., Minocha, S., et al. (2017). WD40-repeat 47, a microtubule-associated protein, is essential for brain development and autophagy. Proc. Natl. Acad. Sci. USA *114*, E9308–E9317. https://doi.org/10.1073/pnas.1713625114.

36. Morikawa, M., Tanaka, Y., Cho, H.S., Yoshihara, M., and Hirokawa, N. (2018). The Molecular Motor KIF21B Mediates Synaptic Plasticity and Fear Extinction by Terminating Rac1 Activation. Cell Rep. *23*, 3864–3877. https://doi.org/10.1016/j.celrep.2018.05.089.

37. Swarnkar, S., Avchalumov, Y., Raveendra, B.L., Grinman, E., and Puthanveettil, S.V. (2018). Kinesin Family of Proteins Kif11 and Kif21B Act as Inhibitory Constraints of Excitatory Synaptic Transmission Through Distinct Mechanisms. Sci. Rep. *8*, 17419. https://doi.org/10.1038/s41598-018-35634-7.

38. Narayanan, D.L., Rivera Alvarez, J., Tilly, P., do Rosario, M.C., Bhat, V., Godin, J.D., and Shukla, A. (2022). Further delineation of KIF21B-related neurodevelopmental disorders. J. Hum. Genet. *67*, 729–733. https://doi.org/10.1038/s10038-022-01087-0.

39. Matsuda, T., and Cepko, C.L. (2007). Controlled expression of transgenes introduced by in vivo electroporation. Proc. Natl. Acad. Sci. USA *104*, 1027–1032. https://doi.org/10.1073/pnas.0610155104.

40. Nishimura, Y.V., Nabeshima, Y.I., and Kawauchi, T. (2017). Morphological and Molecular Basis of Cytoplasmic Dilation and Swelling in Cortical Migrating Neurons. Brain Sci. *7*, 87. https://doi.org/10.3390/brainsci7070087.

41. Brito, C., and Sousa, S. (2020). Non-Muscle Myosin 2A (NM2A): Structure, Regulation and Function. Cells *9*. https://doi.org/10.3390/cells9071590.

42. Hammer, J.A., 3rd, and Burkhardt, J.K. (2013). Controversy and consensus regarding myosin II function at the immunological synapse. Curr. Opin. Immunol. *25*, 300–306. https://doi.org/10.1016/j.coi.2013.03.010.

43. Solecki, D.J., Trivedi, N., Govek, E.E., Kerekes, R.A., Gleason, S.S., and Hatten, M.E. (2009). Myosin II motors and F-actin dynamics drive the coordinated movement of the centrosome and soma during CNS glial-guided neuronal migration. Neuron *63*, 63–80. https://doi.org/10.1016/j.neuron.2009.05.028.

44. Schaar, B.T., and McConnell, S.K. (2005). Cytoskeletal coordination during neuronal migration. Proc. Natl. Acad. Sci. USA *102*, 13652–13657. https://doi.org/10.1073/pnas.0506008102.

45. Tsai, J.W., Bremner, K.H., and Vallee, R.B. (2007). Dual subcellular roles for LIS1 and dynein in radial neuronal migration in live brain tissue. Nat. Neurosci. *10*, 970–979. https://doi.org/10.1038/nn1934.

46. Levet, F., Hosy, E., Kechkar, A., Butler, C., Beghin, A., Choquet, D., and Sibarita, J.B. (2015). SR-Tesseler: a method to segment and quantify localization-based super-resolution microscopy data. Nat. Methods *12*, 1065–1071. https://doi.org/10.1038/nmeth.3579.

47. Bellion, A., Baudoin, J.P., Alvarez, C., Bornens, M., and Métin, C. (2005). Nucleokinesis in tangentially migrating neurons comprises two alternating phases: forward migration of the Golgi/centrosome associated with centrosome splitting and myosin contraction at the rear. J. Neurosci. *25*, 5691–5699. https://doi.org/10.1523/JNEUROSCI.1030-05.2005.

48. Godin, J.D., Thomas, N., Laguesse, S., Malinouskaya, L., Close, P., Malaise, O., Purnelle, A., Raineteau, O., Campbell, K., Fero, M., et al. (2012). p27(Kip1) Is a Microtubule-Associated Protein that Promotes Microtubule Polymerization during Neuron Migration. Dev. Cell *23*, 729–744. https://doi.org/10.1016/j.devcel.2012.08.006.

49. Riedl, J., Crevenna, A.H., Kessenbrock, K., Yu, J.H., Neukirchen, D., Bista, M., Bradke, F., Jenne, D., Holak, T.A., Werb, Z., et al. (2008). Lifeact: a versatile marker to visualize F-actin. Nat. Methods *5*, 605–607. https://doi.org/10.1038/nmeth.1220.

50. Burkel, B.M., von Dassow, G., and Bement, W.M. (2007). Versatile fluorescent probes for actin filaments based on the actin-binding domain of utrophin. Cell Motil Cytoskeleton *64*, 822–832. https://doi.org/10.1002/cm.20226.

51. Broix, L., Jagline, H., Ivanova, E., Schmucker, S., Drouot, N., Clayton-Smith, J., Pagnamenta, A.T., Metcalfe, K.A., Isidor, B., Louvier, U.W., et al. (2016). Mutations in the HECT domain of NEDD4L lead to AKT-mTOR pathway deregulation and cause periventricular nodular heterotopia. Nat. Genet. *48*, 1349–1358. https://doi.org/10.1038/ng.3676.

52. Carabalona, A., Hu, D.J.K., and Vallee, R.B. (2016). KIF1A inhibition immortalizes brain stem cells but blocks BDNF-mediated neuronal migration. Nat. Neurosci. *19*, 253–262. https://doi.org/10.1038/nn.4213.

53. Akkaya, C., Atak, D., Kamacioglu, A., Akarlar, B.A., Guner, G., Bayam, E., Taskin, A.C., Ozlu, N., and Ince-Dunn, G. (2021). Roles of Developmentally Regulated KIF2A Alternative Isoforms in Cortical Neuron Migration and Differentiation. Development *148*. https://doi.org/10.1242/dev.192674.

54. Falnikar, A., Tole, S., and Baas, P.W. (2011). Kinesin-5, a mitotic microtubule-associated motor protein, modulates neuronal migration. Mol. Biol. Cell *22*, 1561–1574. https://doi.org/10.1091/mbc.E10-11-0905.

55. Falnikar, A., Tole, S., Liu, M., Liu, J.S., and Baas, P.W. (2013). Polarity in migrating neurons is related to a mechanism analogous to cytokinesis. Curr. Biol. *23*, 1215–1220. https://doi.org/10.1016/j.cub.2013.05.027.

56. Gilet, J.G., Ivanova, E.L., Trofimova, D., Rudolf, G., Meziane, H., Broix, L., Drouot, N., Courraud, J., Skory, V., Voulleminot, P., et al. (2020). Conditional switching of KIF2A mutation provides new insights into cortical malformation pathogeny. Hum. Mol. Genet. *29*, 766–784. https://doi.org/10.1093/hmg/ddz316.

57. Li, W., Cheng, T., Dong, X., Chen, H., Yang, L., Qiu, Z., and Zhou, W. (2022). KIF5C deficiency causes abnormal cortical neuronal migration, dendritic branching, and spine morphology in mice. Pediatr. Res. *92*, 995–1002. https://doi.org/10.1038/s41390-021-01922-8.

58. Muralidharan, H., Guha, S., Madugula, K., Patil, A., Bennison, S.A., Sun, X., Toyo-Oka, K., and Baas, P.W. (2022). KIFC1 Regulates the Trajectory of Neuronal Migration. J. Neurosci. *42*, 2149–2165. https://doi.org/10.1523/JNEUROSCI.1708-21.2022.

59. Qian, X., DeGennaro, E.M., Talukdar, M., Akula, S.K., Lai, A., Shao, D.D., Gonzalez, D., Marciano, J.H., Smith, R.S., Hylton, N.K., et al. (2022). Loss of non-motor kinesin KIF26A causes congenital brain malformations via dysregulated neuronal migration and axonal growth as well as apoptosis. Dev. Cell *57*, 2381–2396.e13. https://doi.org/10.1016/j.devcel.2022.09.011.

60. Sapir, T., Levy, T., Sakakibara, A., Rabinkov, A., Miyata, T., and Reiner, O. (2013). Shootin1 acts in concert with KIF20B to promote polarization of migrating neurons. J. Neurosci. *33*, 11932–11948. https://doi.org/10.1523/JNEUROSCI.5425-12.2013.

61. Yu, H.L., Peng, Y., Zhao, Y., Lan, Y.S., Wang, B., Zhao, L., Sun, D., Pan, J.X., Dong, Z.Q., Mei, L., et al. (2020). Myosin X Interaction with KIF13B, a Crucial Pathway for Netrin-1-Induced Axonal Development. J. Neurosci. *40*, 9169–9185. https://doi.org/10.1523/JNEUROSCI.0929-20.2020.

62. Lasser, M., Tiber, J., and Lowery, L.A. (2018). The Role of the Microtubule Cytoskeleton in Neurodevelopmental Disorders. Front. Cell. Neurosci. *12*, 165. https://doi.org/10.3389/fncel.2018.00165.

63. Sakakibara, A., Ando, R., Sapir, T., and Tanaka, T. (2013). Microtubule dynamics in neuronal morphogenesis. Open Biol. *3*, 130061. https://doi.org/10.1098/rsob.130061.

64. Witte, H., Neukirchen, D., and Bradke, F. (2008). Microtubule stabilization specifies initial neuronal polarization. J. Cell Biol. *180*, 619–632. https://doi.org/10.1083/jcb.200707042.

65. Schelski, M., and Bradke, F. (2022). Microtubule retrograde flow retains neuronal polarization in a fluctuating state. Sci. Adv. *8*, eabo2336. https://doi.org/10.1126/sciadv.abo2336.

66. Gromova, K.V., Thies, E., Janiesch, P.C., Lützenkirchen, F.P., Zhu, Y., Stajano, D., Dürst, C.D., Schweizer, M., Konietzny, A., Mikhaylova, M., et al. (2023). The kinesin Kif21b binds myosin Va and mediates changes in actin

dynamics underlying homeostatic synaptic downscaling. Cell Reports *42*. https://doi.org/10.1016/j.celrep.2023.112743.

67. Ohtaka-Maruyama, C., Okamoto, M., Endo, K., Oshima, M., Kaneko, N., Yura, K., Okado, H., Miyata, T., and Maeda, N. (2018). Synaptic transmission from subplate neurons controls radial migration of neocortical neurons. Science *360*, 313–317. https://doi.org/10.1126/science.aar2866.
68. Iwai, S., Ishiji, A., Mabuchi, I., and Sutoh, K. (2004). A novel actin-bundling kinesin-related protein from Dictyostelium discoideum. J. Biol. Chem. *279*, 4696–4704. https://doi.org/10.1074/jbc.M308022200.
69. Preuss, M.L., Kovar, D.R., Lee, Y.R.J., Staiger, C.J., Delmer, D.P., and Liu, B. (2004). A plant-specific kinesin binds to actin microfilaments and interacts with cortical microtubules in cotton fibers. Plant Physiol. *136*, 3945–3955. https://doi.org/10.1104/pp.104.052340.
70. Geraldo, S., Khanzada, U.K., Parsons, M., Chilton, J.K., and Gordon-Weeks, P.R. (2008). Targeting of the F-actin-binding protein drebrin by the microtubule plus-tip protein EB3 is required for neuritogenesis. Nat. Cell Biol. *10*, 1181–1189. https://doi.org/10.1038/ncb1778.
71. Ketschek, A., Spillane, M., Dun, X.P., Hardy, H., Chilton, J., and Gallo, G. (2016). Drebrin coordinates the actin and microtubule cytoskeleton during the initiation of axon collateral branches. Dev. Neurobiol. *76*, 1092–1110. https://doi.org/10.1002/dneu.22377.
72. Hebben, M., Brants, J., Birck, C., Samama, J.P., Wasylyk, B., Spehner, D., Pradeau, K., Domi, A., Moss, B., Schultz, P., and Drillien, R. (2007). High level protein expression in mammalian cells using a safe viral vector: modified vaccinia virus Ankara. Protein Expr. Purif. *56*, 269–278. https://doi.org/10.1016/j.pep.2007.08.003.
73. Birling, M.C., Dierich, A., Jacquot, S., Hérault, Y., and Pavlovic, G. (2012). Highly-efficient, fluorescent, locus directed cre and FlpO deleter mice on a pure C57BL/6N genetic background. Genesis *50*, 482–489. https://doi.org/10.1002/dvg.20826.
74. Stenman, J., Toresson, H., and Campbell, K. (2003). Identification of two distinct progenitor populations in the lateral ganglionic eminence: implications for striatal and olfactory bulb neurogenesis. J. Neurosci. *23*, 167–174.
75. Konno, D., Shioi, G., Shitamukai, A., Mori, A., Kiyonari, H., Miyata, T., and Matsuzaki, F. (2008). Neuroepithelial progenitors undergo LGN-dependent planar divisions to maintain self-renewability during mammalian neurogenesis. Nat. Cell Biol. *10*, 93–101. https://doi.org/10.1038/ncb1673.
76. Ovesný, M., Křížek, P., Borkovec, J., Svindrych, Z., and Hagen, G.M. (2014). ThunderSTORM: a comprehensive ImageJ plug-in for PALM and STORM data analysis and super-resolution imaging. Bioinformatics *30*, 2389–2390. https://doi.org/10.1093/bioinformatics/btu202.
77. Xu, T., Langouras, C., Koudehi, M.A., Vos, B.E., Wang, N., Koenderink, G.H., Huang, X., and Vavylonis, D. (2019). Automated Tracking of Biopolymer Growth and Network Deformation with TSOAX. Sci. Rep. *9*, 1717. https://doi.org/10.1038/s41598-018-37182-6.
78. Tyanova, S., Temu, T., Sinitcyn, P., Carlson, A., Hein, M.Y., Geiger, T., Mann, M., and Cox, J. (2016). The Perseus computational platform for comprehensive analysis of (prote)omics data. Nat. Methods *13*, 731–740. https://doi.org/10.1038/nmeth.3901.
79. Skarnes, W.C., Rosen, B., West, A.P., Koutsourakis, M., Bushell, W., Iyer, V., Mujica, A.O., Thomas, M., Harrow, J., Cox, T., et al. (2011). A conditional knockout resource for the genome-wide study of mouse gene function. Nature *474*, 337–342. https://doi.org/10.1038/nature10163.
80. Hand, R., and Polleux, F. (2011). Neurogenin2 regulates the initial axon guidance of cortical pyramidal neurons projecting medially to the corpus callosum. Neural Dev. *6*, 30. https://doi.org/10.1186/1749-8104-6-30.
81. Tielens, S., Godin, J.D., and Nguyen, L. (2016). Real-time Recordings of Migrating Cortical Neurons from GFP and Cre Recombinase Expressing Mice. Curr. Protoc. Neurosci. *74*, 3.29.1–3.29.23. https://doi.org/10.1002/0471142301.ns0329s74.
82. Edelstein, A.D., Tsuchida, M.A., Amodaj, N., Pinkard, H., Vale, R.D., and Stuurman, N. (2014). Advanced methods of microscope control using mu-Manager software. J. Biol. Methods *1*, e10. https://doi.org/10.14440/jbm.2014.36.
83. Li, S., Leshchyns'ka, I., Chernyshova, Y., Schachner, M., and Sytnyk, V. (2013). The neural cell adhesion molecule (NCAM) associates with and signals through p21-activated kinase 1 (Pak1). J. Neurosci. *33*, 790–803. https://doi.org/10.1523/JNEUROSCI.1238-12.2013.
84. Kučera, O., Gaillard, J., Guérin, C., Théry, M., and Blanchoin, L. (2022). Actin-microtubule dynamic composite forms responsive active matter with memory. Proc. Natl. Acad. Sci. USA *119*, e2209522119. https://doi.org/10.1073/pnas.2209522119.
85. Farina, F., Gaillard, J., Guérin, C., Couté, Y., Sillibourne, J., Blanchoin, L., and Théry, M. (2016). The centrosome is an actin-organizing centre. Nat. Cell Biol. *18*, 65–75. https://doi.org/10.1038/ncb3285.

STAR★METHODS

KEY RESOURCES TABLE

REAGENT or RESOURCE	SOURCE	IDENTIFIER
Antibodies		
Rabbit polyclonal anti-Kif21b	Sigma-Aldrich	Cat # HPA027274; RRID: AB_1852483
Mouse monoclonal anti- α-Tubulin (clone DM1A)	Sigma-Aldrich	Cat #T9026; RRID: AB_477593
Rabbit polyclonal anti-Cux1	Sigma-Aldrich	Cat # HPA003317; RRID: AB_2666891
Mouse polyclonal anti-Caspase-3	R&D systems	Cat # AF835; RRID: AB_2243952
Mouse monoclonal anti-Nestin	Abcam	Cat # ab6142; RRID: AB_305313
Rat monoclonal anti-Tbr2	Thermo Fischer Sc	Cat # 14-4875-80; RRID: AB_11043546
Rabbit polyclonal anti-Pax6	Millipore	Cat # ab2237; RRID: AB_1587367
Rat monoclonal anti- Ki67 570 fluorocoupled	ebioscience	Cat # 41-5698-80; RRID: AB_11219874
Goat polyclonal anti-GFP	Abcam	Cat # Ab6673; RRID: AB_305643
Rabbit polyclonal anti-GM130	Protein Tech	Cat# 11308-1-AP, RRID: AB_2115327
Mouse monoclonal anti-Jip-1	Santa Cruz	Cat # Sc-25267; RRID: AB_627838
Rabbit polyclonal anti-Myosin light chain-II	Cell Signaling	Cat # 3672S; RRID: AB_10692513
Mouse monoclonal anti- Actin coupled-HRP	Sigma-Aldrich	Cat # A3854; RRID: AB_262011
Goat anti-rabbit-HRP	Thermo Fischer Sc	Cat # G-21234; RRID: AB_2536530
Goat anti-mouse-HRP	Thermo Fischer Sc	Cat # G-21040; RRID: AB_2536527
Donkey anti-mouse-488	Thermo Fischer Sc	Cat # A-21202; RRID: AB_141607
Donkey anti-goat-488	Thermo Fischer Sc	Cat # A-11055; RRID: AB_2534102
Donkey anti-mouse-555	Thermo Fischer Sc	Cat # A-31570; RRID: AB_2536180
Donkey anti-rabbit-555	Thermo Fischer Sc	Cat # A-31572; RRID: AB_162543
Donkey anti-mouse-647	Thermo Fischer Sc	Cat # A-31571; RRID: AB_162542
Donkey anti-rat-647	Abcam	Cat # ab150155; RRID: AB_2813835
Bacterial and virus strains		
Modified Vaccinia Ankara - MVA	(Hebben et al.)[72]	N/A
Chemicals, peptides, and recombinant proteins		
Poly-L-lysine hidrobromide	Sigma-Aldrich	P2636
Papain	Worthington	LK003178
Ovomucoid inhibitor	Worthington	LK003182-
DnaseI	Roche	04716728001
Recombinant protein: Kif21b	This paper	N/A
Recombinant protein: Actin	Cytoskeleton, Inc.	AKL99-A
Recombinant protein: Actin (for *in vitro* study)	Gift from Laurent Blanchoin	N/A
Para-amino-Blebbistatin	Cayman Chemical	22699
Cytochalasin D	Sigma Aldrich	#C8273
Alexa Fluor™ Plus 647 Phalloidin	Thermo Fisher	A30107
Phalloidin 488 coupled	Thermo Fischer Sc	A12379
B27	Thermo Fischer Sc	17504044
N2	Thermo Fischer Sc	17502048
Penicillin/Streptomycin	Gibco, Life Technologies	15140–130
L-Glutamine	Thermo Fischer Sc	25030–123
Critical commercial assays		
Pierce Protein A/G Magnetic Beads	Thermo-Scientific	88802
Lipofectamine 2000 transfection reagent	Invitrogen	11668019
Neuromag transfection reagent	Oz Biosciences	NM50200

(*Continued on next page*)

Continued

REAGENT or RESOURCE	SOURCE	IDENTIFIER
Deposited data		
Mass spectrometry from immunoprecipitated Kif21b from E18 mouse cortices	This paper	Table S1 ProteomeXchange identifier: PXD042855
Mass spectrometry analysis of fraction of purified recombinant Kif21b protein	This paper	Table S2 ProteomeXchange identifier: PXD042855
Experimental models: Cell lines		
Human: HEK293 cells	ATCC	Cat# 300192/p777_HEK293, RRID: CVCL_0045
Mouse: Neuro-2A cells	ATCC	Cat# CCL-131, RRID: CVCL_0470
Hamster: BHK21C13-2P	ECACC	RRID: CVCL_8837
Experimental models: Organisms/strains		
Mouse: CD1 (WT)	Charles River Laboratories	Strain code: 022
Mouse: NMRI (WT)	Janvier Labs	RjHan:NMRI
Mouse: *Kif21b*$^{Flox/Flox}$ conditional KO mice	International Mouse Phenotyping Consortium	N/A
Mouse: *Kif21b*$^{tm1a(KOMP)Wtsi}$	International Mouse Phenotyping Consortium	RRID:MGI:5781650
Flipase recombinase mouse line (FlpO-2A-eYFP)	Institut Clinique de la souris- (Birling et al.)[73]	N/A
Dlx5,6 Cre-GFP transgenic mice	(Stenman et al.)[74]	N/A
Oligonucleotides		
Kif21b exons 2–3 Forward: AAGGCTGCTTTGAGGGCTAT	This paper	N/A
Kif21b exons 2–3 Reverse: AAAGCCGGTGCCCATAGTA	This paper	N/A
Actin Forward: TATAAAACCCGGCGGCGCA	This paper	N/A
Actin Reverse: TCATCCATGGCGAACTGGTG	This paper	N/A
Kif21b Forward (genotyping): GGGGTACTTTCCATTGACCCAG	This paper	N/A
Kif21b Reverse (genotyping): GAAGGGACCAAACCTGGGC	This paper	N/A
Cre Forward (genotyping): ATCCGAAAAGAAAACGTTGA	This paper	N/A
Cre Reverse (genotyping): ATCCAGGTTACGGATATAGT	This paper	N/A
Recombinant DNA		
Plasmid: NeuroD-mouseKif21b-FL	This paper	N/A
Plasmid: NeuroD-mouseKif21bΔMD (Δ9–371, motor domain)	This paper	N/A
Plasmid: NeuroD- mouseKif21bΔATP (Δ87–94, ATP binding site)	This paper	N/A
Plasmid: NeuroD- mouseKif21bΔWD40 (Δ1308–1639, WD40 domain)	This paper	N/A
Plasmid: NeuroD- mouseKif21b-T96N	This paper	N/A
Plasmid: NeuroD- mouseKif21a	This paper	N/A
Plasmid: pCAGGs-PACT-mKO1	(Konno et al.)[75]	N/A
Plasmid: LifeAct-Ruby	(Riedl et al.)[49]	N/A
Plasmid: GFP-UtrCH	(Burkel, et al.)[50]	RRID:Addgene 26737
Plasmid: Neuro-D:GFP	Gift from F. Polleux	N/A
Plasmid: Neuro-D:Cre	Gift from L.Nguyen	N/A

(*Continued on next page*)

Continued

REAGENT or RESOURCE	SOURCE	IDENTIFIER
Plasmid: pCALSL-mir30-sh-scramble	(Asselin et al.)[25]	N/A
Plasmid: pCALSL-mir30-sh-*Kif21b #1*	(Asselin et al.)[25]	N/A
Plasmid: pCALSL-mir30-sh-*Kif21b #2*	(Asselin et al.)[25]	N/A
Plasmid: pVOTE-Kif21b-6 His	This paper	N/A
Plasmid: pCAG2-Scarlet	Gift from J. Courchet	N/A
Plasmid: pCAG-loxPSTOPloxP-Cherry	Gift from L. Nguyen	N/A
Plasmid: pEGFP-C1-3′UTR KIF21B	(Asselin et al.)[25]	N/A
Plasmid: pEGFP-C1-WT-Kif21b	(Asselin et al.)[25]	N/A
Software and algorithms		
FIJI/ImageJ	Wayne Radband, Nationalinstitute of Health, USA	https://imagej.nih.gov/ij/
ThunderSTORM algorithm	(Ovesny et al.)[76]	https://zitmen.github.io/thunderstorm/
PoCA software	(Levet et al.)[46]	https://github.com/flevet/PoCA https://doi.org/10.5281/zenodo.8017666
TSOAX v 2.0	(Xu et al.)[77]	https://github.com/tix209/TSOAX
GraphPad Prism v6 and v9	GraphPad Software Inc.	https://www.graphpad.com
R Studio version 1.4.1106	RStudio, PBC, Boston, MA URL	http://www.rstudio.com/
Proteome Discoverer 2.4 software	Thermo Fisher Scientific	PD2.4
Perseus	(Tyanova et al.)[78]	https://maxquant.net/perseus/
Metamorph 7.0	Molecular Devices, Downington, PA	https://support.moleculardevices.com/s/
Adobe Illustrator	Adobe Inc.	https://adobe.com/products/illustrator
Other		
Millicell Cell Culture Insert, 30 mm	Millipore	PICMORG50
Magnetic stand	Invitrogen	12321D
Polybeads carboxylate microsphere	Polysciences Europe GMBH	17140–5
35 mm Glass bottom dishes No. 0	MatTek	P35G-0-20-C
Low melting point agarose	Bio-Rad	1613112

RESOURCE AVAILABILITY

Lead contact

Further information and requests for resources and reagents should be directed to and will be fulfilled by the lead contact, Juliette Godin (godin@igbmc.fr).

Materials availability

All information, resources, and reagents listed in key resources table are available from the lead contact upon request.

Data availability

- MS data associated with this work have been deposited to the ProteomeXchange Consortium via the PRIDE partner repository and are publicly available as of the date of publication. Accession number is listed in the key resources table. MS data are available as Tables S1 and S2.
- Plug-in developed to calculate the distances between actin and Kif21b clusters in SMLM data can be found on github (Florian Levet): https://github.com/flevet/PoCA; https://doi.org/10.5281/zenodo.8017666
- Any additional information required to reanalyze the data is available from the lead contact upon request.

EXPERIMENTAL MODEL AND STUDY PARTICIPANT DETAILS

Mice

All animal studies were conducted in accordance with French regulations (EU Directive 86/609 – French Act Rural Code R 214-87 to 126) and all procedures were approved by the local ethics committee and the Research Ministry (APAFIS#15691–201806271458609). Mice

were bred at the IGBMC animal facility under controlled light/dark cycles, stable temperature (19°C) and humidity (50%) condition and were provided with food and water *ad libitum*.

Timed-pregnant wild-type (WT) CD1 (Charles River Laboratories) females were used for *In Utero* electroporation (*IUE*) at embryonic day 13.5 (E13.5), 14.5 (E14.5) and 15.5 (E15.5). NMRI (WT) mice (Janvier Labs) were used for growth cone extraction and actin preparation assays. *Kif21b*$^{tm1a(KOMP)Wtsi}$ were obtained from UC Davis/KOMP repository. Timed-pregnant Dlx5,6 Cre-GFP[74] females were used for ex-vivo electroporation at E13.5 genotyped by PCR detecting the presence of the Cre allele (Oligos can be found in the key resources table). *Kif21b*$^{Flox/Flox}$ conditional KO mice were generated using the International Mouse Phenotyping Consortium targeting mutation strategy[79] by crossing *Kif21b*$^{tm1a(KOMP)Wtsi}$ with a Flipase recombinase mouse line (FlpO-2A-eYFP).[73] Genotyping was done as previously described in.[25] Males an females embryos were indifferently used for the study.

Cell culture

All cells used in this study are provided by the cell culture platform of the IGBMC (Illkirch), are guaranteed mycoplasma free (PCR test Venorgem) and have not been authenticated. Mouse neuroblastoma N2A cells were cultured in DMEM (1 g/L glucose) (Dulbecco's Modified Eagle Medium, GIBCO) supplemented with 5% Fetal Calf Serum (FCS) and Gentamycin 40μg/mL and Human embryonic kidney (HEK) 293T cells were cultured in DMEM (1 g/L glucose) (GIBCO) supplemented with 10% Fetal Calf Serum (FCS), penicillin 100 UI/mL, streptomycin 100 μg/mL in a cell culture incubator (5% CO_2 at 37°C). BHK21 C13-2P cells were grown in Glasgow's modified Eagle's medium (GMEM; Thermo Fisher, MA, USA) supplemented with Bacto Tryptose Phosphate (1.5 g/L), 10% fetal calf serum and 50 μM Gentamycin.

METHOD DETAILS

Cloning and plasmid constructs

shRNAs to deplete the expression of *Kif21b* were directed against the coding sequence 3390–3410 (NM_001252100.1) (sh-*Kif21b #1*) or the 3′-UTR (sh-*Kif21b #2*) and cloned in the pCALSL-mir30[39] backbone vector as described in.[25] Various truncated Kif21b constructs were generated by Sequence and Ligation Independent Cloning (SLIC) as follows: Kif21bΔMD (Δ9–371, motor domain), Kif21bΔATP (Δ87–94, ATP binding site), Kif21bΔWD40 (Δ1308–1639, WD40 domain). The c.288 C>T substitution that abolishes Kif21b mobility was created from WT CDS by site-directed mutagenesis to generate the Kif21b-T96N construct. Wild-type mouse *Kif21a* CDS (NM_001109040.2) was isolated from E18.5 cDNA mouse cortices by PCR and subcloned by restriction-ligation into the NeuroD:IRES-GFP plasmid.[80] pEGFP-C1-WT-Kif21b and pEGFP-C1-3′UTR-Kif21b were cloned as described in (Asselin et al., 2020). The plasmid pCAGGs-PACT-mKO1 bearing the pericentrin-AKAp450 centrosomal targeting (PACT) domain fused to Kusabira Orange was kindly[75] was used to label centrosome and pCAGGS-LifeAct-Ruby[49] and GFP-UtrCH (Burkel, et al. 2007) were used for F-actin labeling. A Cre/*loxP* conditional cherry expressing plasmid pCAG-loxPSTOPloxP-Cherry was used for time-lapse imaging of migrating interneurons. Plasmid DNAs used in this study were prepared using the EndoFree plasmid purification kit (Macherey Nagel).

In utero electroporation

Timed-pregnant mice were anesthetized with isoflurane (2 L per minute (min) of oxygen, 4% isoflurane in the induction phase and 2% isoflurane during surgery: Tem Sega). The uterine horns were exposed, and a lateral ventricle of each embryo was injected using pulled glass capillaries (Harvard apparatus, 1.0OD*0.58ID*100mmL) with Fast Green (1 μg/μL; Sigma) combined with different amounts of DNA constructs using a micro injector (Eppendorf Femto Jet). Embryos were injected with 1 μg/μL of NeuroD:Cre-IRES-GFP vector and 0.5 μg/μL NeuroD:IRES-GFP vector (empty, WT or mutated for Kif21b or WT-Kif21a construct) together with 3 μg/μL of either Cre inducible pCALSL-miR30-shRNA-*Kif21b* or pCALSL-miR30-sh-scramble plasmids. For rescue experiments, 1 μg/μL of truncated Kif21b constructs (or empty plasmid as control) were co-injected with the mentioned plasmids. For time-lapse imaging of actin dynamics, 3 μg/μL of pCAGGS-LifeAct-Ruby plasmid[49] or GFP-UtrCH plasmids (Burkel, et al. 2007) were co-injected. Plasmids were further electroporated into the neuronal progenitors adjacent to the ventricle by discharging five electric pulses (40V) for 50 ms at 950 ms intervals using electrodes (diameter 3 mm; Sonidel CUY650P3) and ECM-830 BTX square wave electroporator (VWR international). After electroporation, embryos were placed back in the abdominal cavity and the abdomen was sutured using surgical needle and thread. Pregnant mice were sacrificed by cervical dislocation, and embryos were collected at E16.5 or E18.5. For postnatal analysis, electroporated pups were killed 2 days after birth (P2) by head sectioning.

In vivo migration analysis

Mouse brain collection, immunolabeling

E16.5 and E18.5 embryos and P2 animals were sacrificed by head sectioning and brains were fixed in 4% paraformaldehyde (PFA, Electron Microscopy Sciences) in Phosphate buffered saline (PBS, HyClone) overnight at 4°C. Dissected brains were embedded in 4% low melt agarose (Bio-Rad), and sectioned with vibratome (Leica VT1000S, Leica Microsystems) in 60 μm slices. Free floating sections were maintained in cryoprotective solution (30% Ethyleneglycol, 20% Glycerol, 30%DH2O, 20% PO_4 Buffer) at −20°C until the time of use. Alternatively, for Cux1, Pax6, Tbr2 and Ki67 immunostaining, after fixation, brains were rinsed and equilibrated in 20%

sucrose in PBS overnight at 4°C, embedded in Tissue-Tek O.C.T. (Sakura), frozen on dry ice and coronal sections were cut at the cryostat (18 μm thickness, Leica CM3050S) and maintained at −80°C until the day of immunolabelling.

Free floating sections were permeabilized and blocked with blocking solution containing 5% Normal Donkey Serum (NDS, Dominic Dutsher), 0.1% Triton X-100 in PBS. Brain slices were incubated with primary antibodies diluted in blocking solution overnight at 4°C and then rinsed and incubated with secondary antibody diluted in PBS-0.1% Triton for 1 h at room temperature (RT). Cell nuclei were stained using DAPI (1 mg/ml Sigma). Slices were mounted in Aquapolymount mounting medium (Polysciences Inc). For Cux1 immunolabeling, antigen retrieval was performed by incubating the sections in boiling citrate buffer (0.01 M, pH 6) for 5 min, followed by standard immunostaining procedure. All primary and secondary antibodies used for immunolabeling are listed in the key resources table.

Images acquisition and analysis

Cell counting were done in at least three different brain slices from of at least three different embryos for each condition. After histological examination, only brains with comparative electroporated regions and efficiencies were conserved for quantification. Analysis of IUE experiments were performed blinded.Images were acquired in 1024x1024 mode using confocal microscope (TCS SP5; Leica) at 20× magnification (z stack of 1.55 μm) and analyzed using ImageJ software. Cortical wall areas (UpCP: upper cortical plate, LoCP: lower cortical plate, IZ/SVZ: intermediate zone, subventricular zone/ventricular zone) were identified according to cell density (nuclei staining with DAPI). The total number of GFP-positive cells in the embryonic brain sections was quantified by counting positive cells within a box of fixed size and the percentage of positive cells in each cortical area was calculated. For quantification of apical (Pax6+) and intermediate progenitors (Tbr2+), a region of interest (ROI) was defined in the area of electroporation (determined by the presence of GFP+ neurons) in IZ or in the SVZ. The number of Tbr2+ among DAPI+, Ki67+ among DAPI+ and Tbr2+Ki67+ among Tbr2+ were counted to determine the number of intermediate progenitors in proliferation in SVZ and IZ. For quantification of apical progenitors, the number of Pax6+ among DAPI+, Ki67+ among DAPI+ and Pax6+Ki67+ among Pax6+ were counted in the ROI delimited in the SVZ.

Organotypic slices and real-time imaging

Organotypic slices *culture*

IUE was performed in CD1 mice as indicated above, E16.5 mouse embryos were killed by head sectioning, and brains were embedded in 4% low-melt agarose (BioRad) diluted in HBSS (Hank's Balanced Salt Solution, ThermoFisher Scientific) and sliced (300 μm) with a vibratome (Leica VT1000S, Leica Microsystems). Brain slices were cultured 16 to 24 h in semi-dry conditions (Millicell inserts, Merck Millipore), in a humidified incubator at 37°C in a 5% CO_2 atmosphere in wells containing Neurobasal medium supplemented with 2% B27 (Thermofisher #17504044), 1% N2 (Thermofisher #17502048), and 1% penicillin/streptomycin (Gibco, Life Technologies). Slice cultures were placed in a humidified and thermo-regulated chamber maintained at 37°C on the stage of an inverted confocal microscope.

Time lapse recordings

Time-lapse confocal microscopy was performed with a Leica SP8 scanning confocal microscope equipped with a 25× water immersion objective/N.A. 0.95 and a humified incubation chamber (37°C, 5% CO_2). 25 successive 'z' optical plans spanning 50 μm were acquired every 30 min for 10 h. Time-lapse acquisitions of actin dynamics in migrating neurons were performed in a confocal Spinning Disk CSU-W1 microscope using a 25X/N.A. 0.95 water immersion objective equipped with a humified incubation chamber, with acquisitions at 10 min intervals for 5 h. Rescue analysis of neuronal migration with para-amino-Blebbistatin (Cayman Chemical, #22699) were done using the same experimental setup except that slices were recorded for 5 h with 20 min intervals, then treated with 3 μM para-amino-Blebbistatin by addition of the drug to the culture media and then recorded for another 5 h.

Analysis of time lapse sequences

All sequences were analyzed using ImageJ by adjusting time-interval in the plugin ''Manual tracking'', as well adjusting the pixel width with the x/y calibration corresponding to the analyzed sequence. Migrating neurons were manually tracked individually during the time-lapse and the data collected were analyzed for migration velocity calculating the mean velocity during the entire time-lapse acquisition; number of pauses was calculated by counting the number of times that the neuron stopped moving (velocity = 0); mean and total duration of pauses were calculated by the mean and total number of minutes in which the neuron spent without moving (velocity = 0), respectively; and motility index was calculated as the mean velocity during the entire time-lapse acquisition subtracting the pausing time (velocity = 0). Analysis of the proportions of multipolar-bipolar, persisting multipolar, bipolar-multipolar and persisting bipolar neurons were done by the identification of migrating neurons with either multipolar or bipolar morphology and the follow-up of morphological changes (or absence of them) during the entire duration of the time-lapse. Swelling and nucleokinesis were counted for each neuron during the time-lapse, as well as the time each neuron took to complete a nucleokinesis. Additionally, nucleokinesis amplitude was measured by tracking the maximum length of the movement of the soma of each bipolar neuron. Branching in the leading process was quantified by counting the number of branches of each neuron in every time point of the time-lapse, followed by the calculation of the mean number of branches and the sum of the minutes that the neuron spent with 2 or more branches. Length of the branches was calculated considering the time point in which the neuron extended at its maximum length the leading process, or main leading process for branching neurons, in which case, the length of all the branches was counted for that time point.

LifeAct-Ruby and GFP-UtrCH fluorescence was determined by delimitating the area of the proximal part of the leading process where the LifeAct signal showed increasing levels and measuring the mean gray values of the delimited region during for each time point of the time-lapse. For each measure, normalization was done with the mean gray fluorescence with a ROI in the soma, where values of fluorescence were constant. Time-lapse analyses were done in at least three different brain slices from different embryos in at least three independent experiments for each condition.

Time lapse imaging of migrating interneurons

Ex-vivo electroporation of medial ganglionic eminence (MGE) and time-lapse imaging has been done as previously described.[81] The heads of E13.5 Dlx5,6 Cre-GFP[74] embryos were harvested, and the cortex removed in order to expose the ganglionic eminences. Plasmids to overexpress Cre inducible pCALSL-miR30-shRNA-*Kif21b* or pCALSL-miR30-sh-scramble were used at a concentration of 3 μg/μL and were directly injected in the MGEs. These plasmids were co-electroporated with a Cre/*loxP* conditional cherry expressing plasmid used at a concentration of 1 μg/μL. Electroporation conditions: 50V, 5 pulses of 50ms duration spaced by 1s interval. Electroporated MGEs were then cultured on cortical cell feeder seeded on glass-bottom Petri dish (MatTek, Ashland, USA). Co-cultures were placed in a humidified and thermo-regulated chamber maintained at 37°C on the stage of an inverted confocal microscope. Time-lapse confocal microscopy was performed with a Leica SP8 scanning confocal microscope with a 25× objective. Images of living cherry-expressing migrating interneurons were acquired every 5 min for 4 h. Migration velocity was analyzed adjusting time interval in the plugin ''Manual tracking'', as well as the x/y calibration with the pixel width of the analyzed sequence. Migrating neurons were manually tracked individually during the time-lapse and the data collected was analyzed for migration velocity. Analyses were done in at least three different embryos in two independent experiments for each condition.

Neuronal culture, fixation and immunostaining

CD1 mice cortices from E15.5 mice were dissected and collected in cold PBS supplemented with BSA (3 mg/mL), MgSO4 (1 mM, Sigma), and D-glucose (30 mM, Sigma). Cortices were dissociated in Neurobasal media containing papain (20U/mL, Worthington) and DNase I (100 μg/mL, Sigma) for 20 min at 37°C, washed 5 min with Neurobasal media containing Ovomucoid (15 mg/mL, Worthington), and manually triturated in OptiMeM supplemented with D-Glucose (20mM). 220 000 cells were plated in Neurobasal Supplemented media supplemented with B27 (Thermofisher #17504044), L-glutamine (2 mM) (Thermofisher #25030-123), and penicillin (5 units/mL) – streptomycin (50 mg/mL) (Thermofisher #15140-130) on round coverslips of N1.H5, 18 mm diameter, pre-coated with Poly-L-Lysine (1 mg/mL). Neurons were incubated in an incubator with controlled CO_2 (5%) and temperature (37°C).

For validation of sh*Kif21b* #2, neurons were magnetofected at *Day in vitro* 1 (DIV1) with 2 μg of plasmid expressing sh-*Kif21b* #2 or sh-Scramble as a control, 0.1 μg of NeuroD-Cre and 0.05 μg of pCAGGS-Venus plasmid using NeuroMag (OZ Bioscience) according to the manufacturer's protocol. At *Day In Vitro* 4, neurons were fixed in PFA 4% for 10 min. Blocking was done in a solution containing BSA 5%, NDS 5% in PBS Triton 0.1% for 1 h. Then neurons were incubated in primary antibody diluted in blocking solution overnight, followed by incubation in secondary antibody coupled to fluorophore Alexa Fluor 555 for 1 h. Finally, neurons were mounted in Aquapolymount.

For cytoskeleton staining, at *Day In Vitro* 2 (DIV2) neurons were incubated with pre-warmed extraction buffer containing 0.25% Triton, 0.1% glutaraldehyde, in PEM buffer (80 mM PIPES, 5 mM EGTA, 2 mM $MgCl_2$, pH 6.8) for 30 s and fixed in a pre-warmed fixing solution containing 0.25% Triton, 0.5% Glutaraldehyde, in PEM buffer. Glutaraldehyde was quenched with 0.1% $NaBH_4$ prepared with phosphate buffer (PB) for 7 min and cells were washed twice with PB. Blocking was performed by incubation with 0.22% gelatine for 2 h at RT with gentle shaking, primary antibody diluted in blocking buffer was incubated at 4°C overnight. Secondary antibody diluted in blocking buffer was incubated 1 h and washed three times with PB. To label F-actin, phalloidin coupled to Alexa Fluor Plus 647 (Invitrogen, A30107) was incubated overnight for aquapolymount mounting for confocal imaging or incubated until the day of acquisition for super resolution microscopy.

Neurons in Figure 4F were imaged using the LiveSR mode of Confocal Spinning Disk CSU-X1 ''Nikon'' equipped with a Photometrics Prime 75B camera and an APO TIRF 100x/N.A. 1.49 oil objective controlled by Metamo0rph 7.10. software.

SMLM imaging protocol

Setup. SMLM was performed with a home-build setup based on an inverted microscope (Eclipse TiE Nikon) equipped with 100x/1.49 NA oil-immersion objective (Apochromat TIRF, Nikon), Perfect Focus and driven with μmanager software.[82] The microscope was equipped with a laser line 532 and 642 nm lasers (Oxxius). Excitation was done in Total Internal Reflection Fluorescence (TIRF) mode to excite only the sample near the surface (<200 nm). A multiband dichroic mirror was used to filter emission from the sample (FF560/659-Di01, Semrock) and notch filters were used to remove scattered laser light (532 nm and 642 nm StopLine single-notch filters: NF01-532U and NF03-642, Semrock). Spectral discrimination of the two different fluorescent probes was achieved by splitting the fluorescence emission on the camera chip by an optical separator (Gemini, Hammatsu associated with a dichroic mirror (FF 640-Di01 Semrock and respectively an LP 532 (Semrock) and an LP 647 (Semrock) for the top and bottom chip areas)). All images were recorded using an EMCCD camera ((C9100-23B ImagEM, Hamamatsu) with 16 × 16 μm pixels), using 240 x 240 top region on the camera for Alexa Fluor 555 labeling and 240 x 240 bottom region for Alexa Fluor 647 labeling.

Chromatic aberration was corrected by imaging TetraSpek fluospheres excited with a low laser power (532nm and 647 nm). A raster scan of a single bead was performed to record a reference image and determined, for each frame, its localization with the

help of DOM ImageJ plugin. This plug-in was also used to determine and corrected the optical and chromatic aberration between the two channels.

Acquisition imaging procedure for SMLM

After neurons were cultured, fixed and immunostained as explained above, the coverslips were placed in an observation chamber (Ludin chamber, LIS) and recovered by fresh 700 μL of imaging solution (prepared just before the use by mixing 7 μL of GLOX buffer (56 mg/mL Glucose oxidase, 3.4 mg/mL catalase, 8 mM Tris 10, 40 mM NaCl 50), 70 μL MEA buffer (1 M MEA in 0.25 N HCl) and 620 μL of buffer containing 50 mM Tris (pH 8.0), 10 mM NaCl and 10% Glucose) to control the redox environment. Acquisition was performed by adjusting the laser power to 50 mW at the objective for both lasers that results in 2 kW/cm^2 excitation intensity and acquisition time to get single fluorophores bursts with the optimal signal-noise ratio. For the dual-color image acquisition, a sequential approach was used with a first dSTORM recording with Alexa Fluor 647 labeling followed by a second dSTORM recording with the Alexa Fluor 555 labeling into two individual image stacks (more than 30 000 frames per stack).

SMLM data analysis

The two sets of images were read by an ImageJ macro, which extracts the appropriate ROI and corrects the chromatic aberrations. Single-molecule localizations in both extract datasets were calculated using the thunderSTORM algorithm.[76] The following parameters were used to find and fit the signal of each particle: image filtering – Difference-of-Gaussians filter (sigma 1 = 1.0 and sigma 2 = 1.6); approximated localization of molecules – Local maximum (peak intensity threshold: std (Wave.F1), connectivity: 8-neighbourhood); sub-pixel localization of molecules – Integrated Gaussian (fitting radius: 4 px, fitting method: Least squares, initial sigma:1.3 px). The reconstructed images of both channels were combined to generate a two colour-image. To calculate the distances between actin and Kif21b clusters, the localization data of the two channels (obtained with ThunderStorm) were analyzed with the PoCA software (https://github.com/flevet/PoCA, plug-in developed by Florian Levet). Single molecule localization coordinates were used to compute a Voronoï tessellation, in order to partition the image space in polygons of various sizes centered on each localized molecule.[46] Using this space-partitioning framework, first-rank densities δ_i^1 of the molecules were computed. Segmentations were performed thresholding these density features with a threshold of 5 times (resp. 2 times) the average density δ of the whole dataset for the Kif21b clusters (resp. actin filaments). Finally, we defined the shortest distance between the Kif21b clusters and the actin filaments as the distance between the clusters' centroid and the closest point of the actin filament borders.

Cell culture and transfections

N2A and HEK293T cell lines were transfected using Lipofectamine 2000 (Invitrogen) according to the manufacturer's protocol. N2A cells were transfected using the different NeuroD:Kif21b-IRES-GFP constructs. HEK293T cells were transfected using sh-scrambled or ShRNA-*Kif21b* #2 together with pEGFP-C1-3′UTR KIF21B or sh-scrambled or ShRNA-*Kif21b* #1 together with pEGFP-C1-WT-Kif21b. Expression of transfected genes was analyzed 48 h after transfection by RT-qPCR or immunoblotting.

Protein extraction and Western blot

Proteins from mouse cortex (E18.5) or transfected cells (N2A or HEK 293T) were extracted as follows: cells were lysed in RIPA buffer (50 mM Tris pH 8.0, 150 mM NaCl, 5 mM EDTA pH 8.0.1% Triton X-100, 0.5% sodium deoxycholate, 0.1% SDS) supplemented with EDTA-free protease inhibitors (cOmplete, Roche) for 30 min, then cells debris were removed by high speed centrifugation at 4°C for 25 min. Protein concentration was measured by spectrophotometry using Bio-Rad Bradford protein assay reagent. Samples were denatured at 95°C for 10 min in Laemmli buffer (Bio-Rad, #1610747) with 2% β-mercaptoethanol (Sigma, #M3148) and then resolved by SDS–PAGE and transferred onto PVDF membranes (Merck, #IPVH00010). Membranes were blocked in 3% milk in PBS buffer with 0.1% Tween (PBS-T) and incubated overnight at 4°C with the antibodies indicated in key resources table diluted in blocking solution. Membranes were washed 3 times in PBS-T and incubated at room temperature for 1 h with the HRP- coupled secondary antibodies indicated in key resources table, followed by 3 times PBS-T washes. Visualization was performed by quantitative chemiluminescence using SuperSignal West Pico PLUS Chemiluminescent Substrate (ThermoFisher, #34580). Signal intensity was quantified using ImageJ.

RNA extraction, cDNA synthesis and RT–qPCR

Total RNA was extracted from the ganglionic eminences of WT NMRI mouse embryos at different time points of development, with TRIzol reagent (Thermo Fisher Scientific). Oligonucleotides to target *Kif21b* ex2-3 and actin cDNAs are listed in the key resources table. RT–qPCR was performed in a LightCycler PCR instrument (Roche) using SYBR Green Master Mix (Roche).

Immunoprecipitation

For immunoprecipitation (IP) experiments, E18.5 brain cortices were lysed using 200 μL of IP buffer (Thermofisher IP Kit (#8788) (1% NP40, 5% Glycerol, 1 mM EDTA, 150 mM NaCl, 25 mM Tris-HCl pH 7.4)) supplemented with EDTA-free protease inhibitors (cOmplete, Roche) and proteins were extracted as explained above. 200 μg of protein were incubated with Kif21b antibody (0.20 μg), actin antibody (2 μg) or corresponding control IgG at 4°C overnight with 5 μL of pre-washed Pierce Protein A/G Magnetic Beads (ThermoScientific, # 88802) (see key resources table for antibodies references). Magnetic beads were collected with a magnetic stand (Invitrogen, 12321D), washed twice with IP buffer and proteins were eluted with 20 μL of Low pH elution buffer (Thermofisher, #1862619) at room temperature for 10 min. Neutralization buffer (Tris pH 8, 1.0 M) and 20 μL of 2x Laemmli Elution Buffer containing 2% β-mercaptoethanol was added to the proteins. Samples were subjected to SDS-PAGE for Western Blot analysis.

Mass spectrometry

Liquid digestion. For mass spectrometry analysis, IP was performed as described above, except that for the protein incubation step, 2 mg of protein,100 μL of pre-washed beads and 3 μg of Kif21b or control IgG antibody were used. After Kif21b elution with 45 μL of low pH elution buffer (Thermofisher, #1862619), the same volume of 2x Laemmli Elution Buffer containing 2% β-mercaptoethanol was added to the sample and the proteins were conserved at −20°C until the analysis. Protein mixtures were precipitated with trichloroacetic acid (TCA) overnight at 4°C, pellets were washed twice with 1 mL cold acetone, dried and dissolved in 8 M urea in 0.1 mM Tris-HCl pH 8.5 for reduction (5 mM TCEP, 30 min), and alkylation (10 mM iodoacetamide, 30 min). Double digestion (LysC - Trypsin) was performed by incubating the proteins first with endoproteinase Lys-C (Wako, #125–05061)) in 8 M urea for 4h at 37°C followed by an overnight trypsin digestion (Promega #V511A) in 2 M urea at 37°C. Peptide mixtures were then desalted on C18 spin-column and dried on Speed-Vacuum before LC-MS/MS analysis.

LC-MS/MS analysis

Samples were analyzed using an Ultimate 3000 nano-RSLC (Thermo Scientific, San Jose California) coupled in line with an LTQ-Orbitrap ELITE mass spectrometer via a nano-electrospray ionization source (Thermo Scientific, San Jose California). One microgram of tryptic peptides (in triplicate) were loaded on a C18 Acclaim PepMap100 trap-column (75 μm ID x 2 cm, 3 μm, 100Å, Thermo Fisher Scientific) for 3.5 min at 5 μL/min with 2% ACN, 0.1% FA in H_2O and then separated on a C18 Accucore nano-column (75 μm ID x 50 cm, 2.6 μm, 150Å, Thermo Fisher Scientific) with a 90 min linear gradient from 5% to 35% buffer B (A: 0.1% FA in H_2O/B: 99% ACN, 0.1% FA in H_2O) followed by a regeneration step (90% B) and a equilibration (5%B). The total chromatography was 120 min at 200 nL/min and at 38°C. The mass spectrometer was operated in positive ionization mode, in Data-Dependent Acquisition (DDA) with survey scans from m/z 350–1500 acquired in the Orbitrap at a resolution of 120,000 at m/z 400. The 20 most intense peaks (TOP20) from survey scans were selected for fragmentation in the Linear Ion Trap with an isolation window of 2.0 Da and were fragmented by CID (Collision-Induced Dissociation) with normalized collision energy of 35%. Unassigned and single charged states were rejected. The Ion Target Value for the survey scans (in the Orbitrap) and the MS2 mode (in the Linear Ion Trap) were set to 1E6 and 5E3 respectively and the maximum injection time was set to 100 ms for both scan modes. Dynamic exclusion was used. Exclusion duration was set to 20 s, repeat count was set to 1 and exclusion mass width was ±10 ppm.

MS data analysis

Proteins were identified with Proteome Discoverer 2.4 software (PD2.4, Thermo Fisher Scientific) and *Mus Musculus* proteome database (Swissprot, reviewed, release 2020_11_20). Precursor and fragment mass tolerances were set at 7 ppm and 0.6 Da respectively, and up to 2 missed cleavages were allowed. Oxidation (M) was set as variable modification, and Carbamidomethylation (C) as fixed modification. Peptides were filtered with a false discovery rate (FDR) at 1%, rank 1. Proteins were quantified with a minimum of 2 unique peptides based on the XIC (sum of the Extracted Ion Chromatogram). The quantification values were exported in Perseus for statistical analysis involving a log[2] transform, imputation, normalization before Volcano plots.[78]

F-actin sedimentation assay

Microdissected E18.5 cortices (3–4 cortices per 500 μL) were lysed in a buffer containing 50 mM PIPES pH 6.9, 50 mM NaCl, 5 mM $MgCl_2$, 5 mM EGTA, 5% glycerol, 0.1% NP40, 0.1% Triton X-100, 0.1% Tween 20, 0.1% β-mercaptoethanol, supplemented with EDTA-free protease inhibitors (cOmplete, Roche) for 10 min at 37°C. The lysate was first centrifuged at 2,000 g for 5 min to remove nuclei then subjected to a high-speed centrifugation (100,000 g, 1 h, 37°C) to obtain a clear supernatant (G-actin) and a pellet (F-actin). Pellet was dissolved overnight at 4°C in water containing 10 μM cytochalasin D (Sigma-Aldrich #C8273) at the same volume as the collected supernatant and equal amounts of each fraction were subjected to Western blot analysis.

Growth cone extraction from mouse brain

Isolation of growth cone was performed on WT NMRI mouse cortices at postnatal day (P) 2 as previously described.[83] Five P2 mouse brains were homogenized in 5 mL of homogenization buffer (5 mM Tris-HCl, 0.32 M sucrose, 1 mM $MgCl_2$) supplemented with EDTA-free protease inhibitors (cOmplete, Roche), then centrifuged at 1,660 x g for 15 min at 4°C. Supernatant were loaded on top of a discontinuous 0.75/1.0/2.33 M sucrose density gradient and centrifuge at 242,000 x g for 60 min at 4°C (Beckman SWTi41 swing rotor). The growth cone depleted fraction was collected between 0.75 M and 1.0 M sucrose. The growth cone enriched fraction was collected at the interface between the load and 0.75 M sucrose, re-suspend in the homogenization buffer and centrifuged at 100,000 *x g* for 40 min at 4°C (Beckman SWTi41 swing rotor). The pellet containing the growth cone were re-suspended in 50 μL of the homogenization buffer. The same volume of each fraction was analyzed by Western blot. Non-growth cone membranes, which also contain Golgi membranes, were revealed by the enrichment of Golgi matrix protein (GM130 primary antibody), while the growth cone fraction was revealed by the enrichment of Jip1 protein.

Purification of human KIF21B

MVA expression vector

A vaccinia virus (strain Modified Vaccinia Ankara[72]- MVA - Bio safe level 1) allowing an inducible expression of mouse Kif21b in mammalian cells (BHK21) were used. Briefly, Kif21b tagged with 6 His-tag at the C-terminal was integrated by homologous recombination at the HA locus of the MVA viral genome.

BHK21 overexpression

For protein production, a 1.8 L preculture of BHK21 C13-2P cells (10^6 cells/ml) grown in Glasgow's modified Eagle's medium (GMEM; Thermo Fisher, MA, USA) supplemented with Bacto Tryptose Phosphate (1.5 g/L), 10% fetal calf serum and 50 μM Gentamycin was infected with approximately 0.1 PFU/cell of recombinant virus and incubated at 37°C. After 48 h, the infected cells were mixed with 6 L of uninfected cells at 10^6 cells/mL at a 1:10 ratio (v/v). Overexpression was induced by the addition of 1 mM IPTG to cell mixture and cells were incubated at 37°C in 5% CO_2 at 75% hygrometry for 24 h. Cells were pelleted at 2000 g for 20 min, washed in PBS and pelleted again at 2000 g for 10 min. Cell pellet was stored at −20°C until use.

KIF21B-6His purification

Pellets from 5L cells were unfrozen and resuspended in lysis buffer (50 mM HEPES pH7.5, 500 mM NaCl, 1 mM $MgCl_2$, 10 mM Imidazole, 0.5% IGEPAL CA-630, 2 mM β-Mercapto-ethanol supplemented with Roche cOmplete inhibitor cocktail tablets) at a ratio of 15 mL of buffer/g of biomass. Lysis was performed by pulse sonication on ice (5 min with pulses 2s ON, 2s OFF). Lysate was then clarified by ultracentrifugation for 1 h at 100.000 g at 4°C. After filtration on cellulose filter 5μm, the supernatant was loaded on HisTrap Excel 5mL column (Cytivia). Column was washed with 10 mM imidazole and proteins were eluted with a gradient from 10 to 500 mM of imidazole. Peak fractions at 280 nm were analyzed on SDS-PAGE and fractions containing the complex were pulled together. The sample was then concentrated using an Amicon Ultra 15 mL with a 100-kDa molecular weight cutoff (MWCO) and further purified using a HiLoad Superdex 200 pg 16/60 column (Cytivia) equilibrated with GF buffer (10 mM HEPES pH7.5, 250 mM NaCl, 1 mM $MgCl_2$, 2 mM DTT). 2 fractions containing the purest complex (checked by SDS-PAGE) were pooled together to obtain two pooled recombinant sample, concentrated using an Amicon Ultra 15 mL with a 100-kDa molecular weight cutoff (MWCO) to 0.7 mg/mL, flashed frozen in liquid nitrogen and stored at −80°C. The contaminants found in the two pooled samples can be found in Table S2.

In vitro co-sedimentation assays

Actin was polymerized according to the manufacturer instructions with some modifications to prepare F-actin at 21 μM. Briefly, actin (Cytoskeleton, #AKL99-A) was resuspended in general actin buffer (5 mM Tris-HCl pH 8.0 and 0.2 mM CaCl2), and incubated 30 min at 4°C. Actin polymerization buffer (500 mM KCl, 20 mM $MgCl_2$, 10 mM ATP) was added and incubated 1 h at 24°C.

The binding experiments were performed for the following conditions: Kif21b alone and Kif21b+Actin; using 5 μL of recombinant Kif21b (from fraction 1), 29 μL of polymerized actin and adding actin buffer to complete a volume of 50 μL. The reactions were incubated 30 min at 24°C and ultracentrifuged 60 min at 60 000 rpm in an Optima MAX-E Ultracentrifuge, using the rotor TLA 100.4. Supernatant was collected and resuspended in 10 μL of 4x Laemmli buffer containing 2% β-mercaptoethanol, while the pellet was resuspended adding 30 μL of milliQ water followed by 30 μL of 2% β-mercaptoethanol. Pellet and supernatant fractions were then analyzed by Coomassie staining. After running the samples in an SDS-PAGE gel, the gel was warmed for 40 s in a microwave in a solution containing 50% ethanol, 10% acetic acid, and incubated on agitation at RT for 10 min. It was then incubated overnight in a solution containing 5% ethanol and 7.5% acetic acid with Coomassie blue. The gels were washed in milliQ water to remove background.

Actin polymerization assays *In vitro*

Coverslips preparation

Glass coverslips were oxidized with oxygen plasma (30s,35%, Diener Electronic, cat. ZeptoB) and incubated with 5% BSA in HEPES 10 mM at pH 7.4 for 10 min RT and washed with HEPES 10 mM.

Actin polymerization of cortices extract

Actin (Gift from Laurent Blanchoin[84]) assembly was induced by mixing 7,36 μL of cortex extract with the reaction mixture containing 18 μL fluorescent buffer (15 mM imidazole, pH 7.0, 74 mM KCl, 1.5 mM $MgCl_2$, 165 mM DTT, 2 mM ATP, 50 mM $CaCl_2$, 5 mM glucose, 30 mg/mL catalase, 155 mg/mL glucose oxidase, and 0.75% methylcellulose.), 2.64 μL of G buffer (2mM Tris-HCl, 0.2 mM Na_2 ATP, 0.2 mM $CaCl_2$, 5 mM DTT), 0.1% BSA and 1 μL of phalloidin 488 nm (A12379,1/200, diluted in HEPES 10 mM). 5 μL of the reaction mixture were immediately put between coated-coverslip and slide and sealed with VALAP (1:1:1 vaseline, lanolin and paraffin).

Actin polymerization with purified protein

Actin assembly (1 μM) was induced by mixing TicTac buffer[85] (10 mM HEPES,16 mM PIPES, 50 mM KCl, 5 mM MgCl2,1 mM EGTA supplemented with - 2.7 mM ATP, 10 mM DTT, 20 μg/mL Catalase, 3 mg mL Glucose, 100 μg/mL Glucose Oxydase, 0.25% Methycellulose) with 0.1% BSA and 1/60 000 phalloidin (Fisher Scientific A12379). Kif21b (from fraction 2) was added at a final concentration of 1 nM or 10 nM. Alternatively, for the polymerization assays on beads, 2μL of beads prepared as follows were used: 10μL of beads (4.5μm - Polybeads carboxylate microsphere, polyscience #17140-5) were centrifuged and the pellet was resuspended in 100μL of Xb buffer (100 mM KCl, 0.1 mM CaCl2, 2 mM MgCl2, 5mm EGTA, 10mm HEPES) in absence or presence of recombinant Kif21b (100 nM). The beads were left for 30 min at RT 700RPM and then centrifuged at 10 000 RPM for 2 min. The pellet was resuspended in 200μL of 1% BSA (diluted in Xb) for 15 min on ice. The beads were centrifuged at 10 000 RPM for 2 min, then the pellet was resuspended in 20μL of 0.1% BSA (diluted in Xb).

In both cases, the reaction mixture was immediately put in a flow chamber (constitute of clean glass slide, a BSA-coated coverslip, and precut adhesive double tape 50 μm thick) and sealed with VALAP (1:1:1 vaseline, lanolin and paraffin).

Bundling assay

Pre-polymerisation of actin filaments in TicTac buffer[85] is performed independently in two tubes for 20 min to obtain two labeled filament populations of different colors. The first filament population is labeled with Phalloidin 488 (1/60,000). The second solution is composed of Alexa 568 fluorescent actin in presence or not of Kif21b (1nM). Phalloidin 488 filaments are then incubated in a home-made microscopy chamber (consisting of a clean glass slide, coverslip and 50 μm thick double sided adhesive tape) allowing them to adhere on the glass surface. After washing with G buffer (2mM Tris-HCl, 0.2 mM Na_2 ATP, 0.2 mM $CaCl_2$, 5 mM DTT), the second population of actin-Alexa568 filaments was added (with or without Kif21b) and left 15 min at room temperature to allow interaction with the immobilised filament population before a soft washing step. Observation were then performed using spinning disk microscopy.

Image acquisition

Images were taken using an inverted Nikon EclipseTi microscope equipped with a ×100 oil objective (HCX plan APO) and a Photometrics Prime 95B (Teledyne Photometrics). The microscope and devices were driven by MetaMorph (Molecular Devices, Downington, PA). Images of actin polymerization of cortices extract were acquired every 1s with the following parameters: 30% of laser power and 200ms of exposure time. Image of actin polymerization with purified proteins were acquired every 5s with the following parameters: 50% of laser power and 100ms of exposure time. For actin polymerization assays on beads, images at spinning disk were taken after 10 min of polymerization. For each condition, between 31 and 36 beads were analyzed. For actin bundling, between 15 and 11 images from 3 independent experiment were taken under using an inverted Nikon EclipseTi microscope.

Image analysis

Filaments were segmented using TSOAX (V0.2.0, default parameters except for Gaussian-std: 2 and by adjusting the ridge threshold).[77] The resulting file was treated using a home-made script on R studio (Version 1.4.1106). The results were plot using a Prism 9. The total amount of polymerized actin was calculated as the sum of all filaments detected at each time. Then, the mean amount of polymerized actin was plotted, the linear regression was calculated, and statistical differences were calculated with GraphPad Prism 9. Mean length of all the detected filaments was measured at each time point. The results were analyzed by fitting the exponential curve and statistical differences was calculated with Prism 9. To quantify actin elongation rate, single filaments were manually tracked: filament length was measured during 90s. The results were plotted, and the linear regression was calculated, and statistical differences was calculated with GraphPad Prism 9. To assess the level of specific actin polymerization of the beads, an area of interest was drawn on the bead and the intensity was measured. This average intensity was compared to an area of interest of the same size next to the bead. To quantify actin bundles in each condition, at least, 33 filaments from at least 3 different experiments were randomly selected and the fluorescence along the filament plotted using the Fiji "plot profile" function. Filaments showing non-homogeneous fluorescence (sudden high intensity) or showing forks less intense than the rest of the filaments were considered as bundles. The co-localization value was calculated as Pearson's correlation coefficient using colocalization tool of Fiji.

QUANTIFICATION AND STATISTICAL ANALYSIS

Quantification of data are described under various Methods sections where applicable. All statistics were calculated using GraphPad Prism 6 or 9 (GraphPad) and are represented as mean ± s.e.m. The number of experiment repetitions and statistical tests are indicated in the figure legends and also reported in Data S1. Adjustments made for multiple comparisons, confidence intervals and exact p-values for Figure 1B, 1E, 1G and 1I; 2D–K, 2M–P, 2R-W; 3C, 3E–J; 4H, 4J, 4L–O; 5B–C, and 5G–5T; S1A, 1B, S1D, S1F, S1I, S1L; S2A, S2B, S2D; S3C; S4C, S4D, S4G, S4H; and S55B, S5G–S5T are reported in Data S1. Graphs were generated using GraphPad and images were assembled with Adobe Illustrator CS6 (Adobe Systems).